Liquefaction Modeling for Biocemented Calcareous Sand

Yang Xiao, M.ASCE[1]; Zhichao Zhang[2]; Armin W. Stuedlein, M.ASCE[3]; and T. Matthew Evans, M.ASCE[4]

Abstract: A thermodynamics-based constitutive model is developed for calcareous sand treated by microbially induced calcite precipitation (MICP) to describe the effects of biocementation and its degradation by cyclic shearing within the framework of nonequilibrium thermodynamics. The elastic potential function implemented within the constitutive model leads to a hyperelastic representation of stress-strain-strength with considerations of true cohesion and stress-density state dependency, yielding a theoretical stress state boundary surface for sands treated with different levels of MICP. In addition, the concepts of configuration entropy and locked energy are defined to describe energy dissipation and corresponding irreversible deformation accumulated during cyclic loading. The effects of MICP treatment on the cyclic behavior of sands can be well predicted through the definition of the MICP-induced increase in soil density and a bonding parameter that varies as a function of the reaction index, representing the concentration and volume of microbial reactant. Predictions of a series of undrained cyclic triaxial tests of sands with and without MICP are made to validate the model. It is shown that a two-stage degradation of the bonding between sand particles should be considered for better predictions of the cyclic behavior. In general, the model sufficiently captures the cyclic stress-strain hysteresis and excess pore pressure generation in MICP-treated sand and gives insights into the underlying mechanisms. **DOI: 10.1061/(ASCE)GT.1943-5606.0002666.** © *2021 American Society of Civil Engineers.*

Introduction

Taking advantage of the urea hydrolysis induced by bacteria-induced urease, the microbially induced calcite precipitation (MICP) process can be realized efficiently within a short time in sands with a suitable solute environment within soil pores (Whiffin 2004; DeJong et al. 2006; Whiffin et al. 2007; van Paassen 2009; van Paassen et al. 2010; Li et al. 2016; Mujah et al. 2017). The calcium carbonate ($CaCO_3$) precipitated at the soil particle contacts and on the particle surfaces will significantly improve the physical and mechanical properties of sand, enlarging the particle size, decreasing the void ratio, forming interparticle bonds, and increasing particle surface roughness (Al Qabany et al. 2012; Montoya and DeJong 2015; O'Donnell and Kavazanjian 2015; Pham et al. 2018; Gao et al. 2019; Nafisi et al. 2019; Xiao et al. 2019c; Ma et al. 2021). The effects of MICP on the mechanical behavior of sand have been studied widely in laboratory tests. Feng and Montoya (2016), Lin et al. (2016), Cui et al. (2017), Terzis and Laloui (2019), and He et al. (2020) studied the effects of MICP cementation level on the strength and dilatancy of biocemented sand; Gomez et al. (2018) reported the results of large-scale laboratory tests on the cone penetration properties of MICP-treated sand; and Xiao et al. (2020a) examined the effect of MICP on compressibility and reduction in grain crushing and thereby its application in pile engineering to improve the bearing capacity (Xiao et al. 2020b). In addition, particle size (Mahawish et al. 2018; Nafisi et al. 2020) and particle shape (Xiao et al. 2019b; Song et al. 2021) could influence the mechanical properties of MICP-treated soils, hence soil properties need to be considered in such applications. Due to the significant effects of MICP on the strength and permeability of granular matter, applications of MICP in desertification control (Gomez et al. 2015; Duo et al. 2018; Li et al. 2020), dust suppression (Naeimi and Chu 2017), and erosion prevention (Salifu et al. 2016; Jiang and Soga 2017; Jiang et al. 2017; Tian et al. 2018; Wang et al. 2018; Jiang et al. 2019; Fattahi et al. 2020; Liu et al. 2020) have also been studied. For the issue of liquefaction mitigation concerned in this paper, it had been reported that MICP-treated sand exhibits a remarkably higher resistance to cyclic liquefaction (Montoya et al. 2013; Riveros and Sadrekarimi 2020a). Due to the ability of cohesionless soils to readily absorb injected bacterial and reactant solutions, MICP provides a suitable and highly efficient approach for the mitigation of liquefaction at developed and undeveloped sites. Numerous laboratory investigations have been implemented to evaluate the dynamic responses of MICP-treated liquefiable soils (Sasaki and Kuwano 2016; Feng and Montoya 2017; O'Donnell et al. 2017a; Simatupang et al. 2018; Xiao et al. 2018; Darby et al. 2019; Zamani and Montoya 2019; Riveros and Sadrekarimi 2020b). Recently, Xiao et al. (2019a) reported a series of undrained cyclic triaxial tests studying the effect of initial relative density on the cyclic behavior of calcareous sand treated with different levels of MICP. However, the detailed mechanical mechanisms controlling the cyclic behavior of MICP-treated sand and its constitutive modeling remain relatively understudied. It has been shown that MICP-treated sand exhibits distinct cyclic responses as compared with the untreated sand (Montoya et al. 2013; Sasaki and Kuwano 2016; O'Donnell et al. 2017b; Xiao et al. 2019a), which presents significant necessity to establish an appropriate constitutive model for implementation within numerical analyses.

The development of constitutive models within critical state framework for structured clays and artificially bonded, cement-treated,

[1]Professor, Key Laboratory of New Technology for Construction of Cities in Mountain Area, State Key Laboratory of Coal Mine Disaster Dynamics and Control, School of Civil Engineering, Chongqing Univ., Chongqing 400045, China. Email: hhuxyanson@163.com

[2]Associate Professor, School of Civil Engineering, Chongqing Univ., Chongqing 400045, China (corresponding author). Email: zhangzhichaopt@163.com

[3]Professor, School of Civil and Construction Engineering, Oregon State Univ., Corvallis, OR 97331. ORCID: https://orcid.org/0000-0002-6265-9906. Email: Armin.Stuedlein@oregonstate.edu

[4]Professor, School of Civil and Construction Engineering, Oregon State Univ., Corvallis, OR 97331. Email: matt.evans@oregonstate.edu

Note. This manuscript was submitted on October 7, 2020; approved on July 7, 2021; published online on September 25, 2021. Discussion period open until February 25, 2022; separate discussions must be submitted for individual papers. This paper is part of the ***Journal of Geotechnical and Geoenvironmental Engineering***, © ASCE, ISSN 1090-0241.

and gypsum-treated soils (Kasama et al. 2000; Rouainia and Muir Wood 2000; Baudet and Stallebrass 2004; Lee et al. 2004; Yu et al. 2007; Suebsuk et al. 2010, 2011; Yan and Li 2011) provides a basis to establish an appropriate constitutive model for MICP-treated sand (Porcino and Marcianò 2017). However, the constitutive model of bonded geomaterials subjected to cyclic loading remains a challenge for geotechnical engineers and researchers. Existing cyclic constitutive models for unbonded sands or clays are usually developed within the framework of classical elastoplasticity. Among these models, the generalized plasticity (Pastor et al. 1990), multiyield surface model (Mroz 1967; Yang and Elgamal 2008), and bounding surface model (Dafalias and Popov 1976; Bardet 1990; Manzari and Dafalias 1997; Xiao et al. 2014; Ziotopoulou 2014) have been developed to model the cyclic liquefaction or cyclic mobility of soils, allowing plastic strain accumulation in the unloading and reloading processes. Zhang and Wang (2012) proposed a constitutive model for predicting large postliquefaction deformations of sand by decomposing the volumetric strain into different specific components. More complexly, rotational yield surfaces (Zheng 2015) or fabric parameters (Li and Dafalias 2012; Rahimi et al. 2016) are introduced to consider the effects of stress-induced anisotropy on the cyclic soil behaviors. Cyclic constitutive models have been coupled with hypoplasticity (Wang and Ma 2019) or the critical state model with a kinetic hardening rule (Barrero et al. 2020) to improve their ability to reproduce observed response. These models provide an effective way to capture the cyclic response of sands but require additional laws for yield surfaces or the evolution of bounding surfaces. Consideration of the effects of particle bonds in cyclic shear can therefore pose a challenging task.

Alternatively, the nonequilibrium thermodynamic theory (Groot and Mazur 1962) provides an effective framework to develop a cyclic constitutive model for soils (Zhang and Cheng 2015; Zhang 2017). More recently, Zhang et al. (2021) proposed a thermodynamic constitutive model for bonded and unbonded soils. However, this model was mainly developed for modeling soil behavior under monotonic loading rather than cyclic loading, and hardly used for modeling bonded soils under cyclic loading, as the residual elastic energy [or the frozen elastic energy (Collins 2005)] and the degradation of bond (precipitated $CaCO_3$) structure have not been fully considered. Therefore, an enhanced nonequilibrium thermodynamic approach is employed in this paper to derive a cyclic constitutive model, which is proposed herein for MICP-treated sand. Based on the fundamental considerations of the energy potential and dissipation, as well as the degradation of the bond structure and corresponding cohesion reduction, the proposed model can capture both the prefailure and postfailure behavior of MICP-treated sand under cyclic loading. A reaction index representing the concentration and volume of the urea-calcium solution used in the MICP process is incorporated into the model to predict the behavior of sands treated with different levels of MICP.

Cyclic Constitutive Theory for MICP-Treated Sand

A cyclic constitutive model for MICP-treated sand based on thermodynamics is presented here. For simplification, it is assumed that the sand is an initially isotropic material and only stress-induced anisotropy is considered under cyclic loading. Following the concepts of configuration entropy and temperature in thermodynamics (Valanis et al. 1993; Evans and Frost 2010; Evans and Brown 2014; Preisler and Dijkstra 2016), the granular configuration temperature T_c is employed here to consider the effect of granular configuration on the mechanical responses of sand. Within this concept, sand liquefaction results from the transition of a granular element from granular solid state to granular liquid (liquefied) state when T_c increases to a threshold value T_{ct} due to density reduction or undrained shearing. A detailed introduction of T_c can be found in the Supplemental Materials.

State-Dependent Hyperelastic Relations

In hyperelasticity, elastic constitutive relations are given by the effective stress tensor, $\sigma'_{ij} = \partial\omega_e/\partial\varepsilon^e_{ij}$, where ω_e is the macroelastic potential density; and ε^e_{ij} is the elastic strain tensor. For granular matter, elasticity vanishes when the solid volume fraction becomes too low or the granular microstructure becomes too weak to enable elastic interactions among granular particles, leading to the granular liquid states (i.e., $T_c \to T_{ct}$) at which $\sigma'_{ij} = 0$. Thus, the following new hyperelasticity-based effective stress principle, which depends on T_c, can be defined from thermodynamics to provide a unified treatment of the elasticity of granular matter at different states

$$\sigma_{ij} = \sigma'_{ij} + u\delta_{ij}, \sigma'_{ij} = (1 - T_c/T_{ct})\sigma^e_{ij}, \sigma^e_{ij} = \partial\omega_e/\partial\varepsilon^e_{ij} \quad (1)$$

where σ_{ij} and σ^e_{ij} = total and elastic stress tensors, respectively; u = pore pressure; and δ_{ij} = Kroneker delta. The elastic energy potential density ω_e is usually defined as a function of the following strains:

$$\varepsilon^e_v = \varepsilon^e_{ij}\delta_{ij} = \varepsilon^e_{ii}, \qquad \varepsilon^e_s = \sqrt{e^e_{ij}e^e_{ij}}$$
$$\varepsilon^e_t = \sqrt[3]{e^e_{ij}e^e_{jk}e^e_{ki}}, \qquad e^e_{ij} = \varepsilon^e_{ij} - \varepsilon^e_v\delta_{ij}/3 \quad (2)$$

where ε^e_v = elastic volumetric strain; and ε^e_s and ε^e_t = second and third invariants of the deviatoric elastic strain tensor e^e_{ij}.

Zhang and Cheng (2015) derived a function of elastic potential for soils, in which a cohesion-related strain index ε_c was introduced to account for the bonding-induced tensile strength in the strain space. Based on a similar approach, the stress-induced anisotropy of elasticity associated with the third elastic strain invariant and the bonded structural potential are further considered in this study. To this end, a bond (precipitated $CaCO_3$) structure index ε_{bs} is defined here to describe the elastic structural potential resulting from the friction and interlocking within bonded materials in the strain space. Therefore, ω_e is defined here in terms of elastic strain invariants as well as ε_c and ε_{bs}

$$\omega_e = B(\varepsilon^e_v + \varepsilon_c)^m\left[\frac{\varepsilon^e_v - \varepsilon_c/(m+1)}{(m+2)/(\varepsilon^e_v + \varepsilon_c)} + \xi(\varepsilon^e_s)^2\right] + B\frac{(\varepsilon_c)^{m+2}}{(m+2)(m+1)} + B\theta\frac{(\varepsilon^e_t)^3}{(\varepsilon^e_s)^{1-m}} + B\frac{(\varepsilon_{bs})^{m+2}}{m+2} \quad (3)$$

where the first two terms on the right side were proposed in Zhang and Cheng (2015) by defining $[K_e, G_e] \propto (\varepsilon^e_v + \varepsilon_c)^m$ with a nonlinear index m (where K_e and G_e are the elastic bulk and shear moduli, respectively); the third term with ε^e_s and ε^e_t = elastic potential leading to the stress-induced anisotropy of elasticity (Xiao et al. 2020c); and the last term = bonded structural potential, simply defined as a power function of ε_{bs}. In Eq. (2), B is a stress-dimensioned parameter for elastic modulus, described below; and ξ and θ are two dimensionless material constants quantifying the bulk and shear moduli. It should be noted that ε_c and ε_{bs} will eventually vanish when the cohesion and bond structure are fully destroyed under cyclic loading. Substituting Eq. (3) into Eq. (1) results in the following analytical nonlinear hyperelastic relationship for MICP-treated sand:

$$\sigma'_{ij} = (1 - T_c/T_{ct})\sigma^e_{ij} = (1 - T_c/T_{ct})(p_e\delta_{ij} + S^e_{ij})$$
$$p_e = B(\varepsilon^e_v + \varepsilon_c)^m \varepsilon^e_v + Bm\xi(\varepsilon^e_v + \varepsilon_c)^{m-1}(\varepsilon^e_s)^2$$
$$S^e_{ij} = [2\xi(\varepsilon^e_v + \varepsilon_c)^m - (1-m)\theta(\varepsilon^e_t)^3/(\varepsilon^e_s)^{1-m}] \times Be^e_{ij} + (3B\theta/(\varepsilon^e_s)^{1-m})[e^e_{ik}e^e_{kj} - (\varepsilon^e_s)^2\delta_{ij}/3] \quad (4)$$

where p_e and S^e_{ij} = elastic pressure and elastic deviatoric stress tensor, respectively. Eq. (4) can be reduced to a nonlinear expression for untreated sands with $\varepsilon_c = 0$. Furthermore, the parameter B should be regarded as a density-dependent variable to describe the effect of density on the elastic stiffness and strength for both bonded and unbonded sands, and is given by

$$B = B_0 e^{k\rho} \quad (5)$$

where B_0 = material constant with a dimension of stress; k = parameter that controls the density dependency of elastic behavior; and ρ = dry density of the MICP-treated sand.

It should be noted that Eq. (2) only gives the macroelastic potential that can be simultaneously released upon the unloading of macroeffective stress. There also exists elastic potential locked within the force network within a sand matrix as a result of plastic deformation (Zhang and Cheng 2015), which is defined as residual elastic potential in this study (also called locked energy or frozen elastic energy) (Palmer 1967; Jefferies 1997; Collins 2005; Yan and Li 2011). Similarly, the residual elastic strain tensor, denoted as ε^r_{ij}, can be defined as another state variable for the definition of residual elastic potential density ω_r. Its conjugate state variable is the residual stress tensor σ^r_{ij}, determined by $\sigma^r_{ij} = \partial\omega_r/\partial\varepsilon^r_{ij}$. Following the hyperelastic model proposed by Houlsby et al. (2005), the definition of ω_r is given by

$$\omega_r = [B/(m+2)][(\varepsilon^r_v)^2 + \xi(\varepsilon^r_s)^2]^{(1+m/2)}$$
$$\varepsilon^r_s = \sqrt{e^r_{ij}e^r_{ij}}, \qquad \varepsilon^r_t = \sqrt[3]{e^r_{ij}e^r_{jk}e^r_{ki}}, \qquad e^r_{ij} = \varepsilon^r_{ij} - \varepsilon^r_v\delta_{ij}/3 \quad (6)$$

where $\varepsilon^r_v(=\varepsilon^r_{kk})$ = residual elastic volumetric strain; and ε^r_s and ε^r_t = second and third invariants of the residual elastic-deviatoric strain tensor, e^r_{ij}, respectively. Then, the residual stress takes the form of

$$\sigma^r_{ij} = B[(\varepsilon^r_v)^2 + \xi(\varepsilon^r_s)^2]^{\frac{m}{2}}(\varepsilon^r_v\delta_{ij} + \xi e^r_{ij}) \quad (7)$$

where the third invariant ε^r_t is not considered. The macroelastic potential and the residual elastic potential are considered to be independent from each other, so that σ^r_{ij} does not directly contribute to the macroelastic effective stress. However, σ^r_{ij} significantly affects both the monotonic and cyclic inelastic behavior of sand, as will be presented below.

Plastic Laws and Degradation of MICP Bonding

According to Eq. (1), all elasticity would disappear for sands in a fluid state with a granular configuration temperature $T_c = T_{ct}$. Therefore, a more generalized definition for the strain rate components within the thermodynamic paradigm should be considered as

$$(1 - T_c/T_{ct})\dot{\varepsilon}_{ij} = \dot{\varepsilon}^e_{ij} + \dot{\varepsilon}^{gp}_{ij} \quad (8)$$

where ε^{gp}_{ij} = generalized plastic strain tensor different from the common concept of plastic strain when taking T_c into account. When $T_c = T_{ct}$, the elastic strain will approach zero at a rate of $\dot{\varepsilon}^{gp}_{ij}$ [i.e., Eq. (8) is reduced to $\dot{\varepsilon}^e_{ij} = -\dot{\varepsilon}^{gp}_{ij}$]. The sand at such a state will then deform like a fluid of suspended particles without effective stress (Uzuoka et al. 1998; Wang et al. 2020). For MICP-treated sand, this can occur if the bonded particle structure is totally destroyed due to shearing. Eq. (8) in fact implies a total inelastic strain rate of $\dot{\varepsilon}^{ie}_{ij} = \dot{\varepsilon}^{gp}_{ij} + (T_c/T_{ct})\dot{\varepsilon}_{ij}$, in which the term $(T_c/T_{ct})\dot{\varepsilon}_{ij}$ can be referred to as a configuration strain rate.

Following the thermodynamic theory proposed by Zhang and Cheng (2015) and Zhang (2017), the generalized plastic strain rate of tensor ε^{gp}_{ij} can be defined as a function of $(\varepsilon^e_{ij} - \varepsilon^r_{ij})$ to consider the increased resistance of material to plastic deformation due to the residual stress. This results in

$$\dot{\varepsilon}^{gp}_{ij} = \Theta(\varepsilon^e_v + \varepsilon_c)^m \times [\lambda_v(\varepsilon^e_v - \varepsilon^r_v - \alpha(\varepsilon^e_s)^2/(\varepsilon^e_v + \varepsilon_c))\delta_{ij} + \lambda_s(e^e_{ij} - e^r_{ij})] \quad (9)$$

where λ_v and λ_s = dissipative coefficients for inelastic volumetric and shear strains, respectively; the term $-\alpha(\varepsilon^e_s)^2/(\varepsilon^e_v + c)$ determines the plastic volumetric strain rate induced by shear dilation; and the dilation index α is related to the critical state line (CSL). To ensure that all dissipation of energy ceases upon cessation of strain, a strain rate factor Θ is defined as

$$\Theta = \sqrt{\dot{\varepsilon}^2_v + \dot{\boldsymbol{e}}_{ij}\dot{\boldsymbol{e}}_{ij}} \quad (10)$$

where $\dot{\varepsilon}_v$ = volumetric strain rate; $e_{ij}(=\varepsilon_{ij} - \varepsilon_v\delta_{ij}/3)$ = deviatoric strain tensor; and $\dot{\boldsymbol{e}}_{ij}$ = deviatoric strain tensor rate.

It is known that the generation and dissipation of residual elastic potential can only develop in response to plastic deformation (Collins 2005). Therefore, based on the thermodynamic approach (Zhang and Cheng 2015), a production term $\dot{\varepsilon}^{gp}_{ij}$ and a dissipation term in proportion to ε^r_{ij} can be defined in the expression of the residual elastic strain rate as follows:

$$\dot{\varepsilon}^r_{ij} = \begin{cases} \overset{\text{production}}{\dot{\varepsilon}^{gp}_{ij}} - \overset{\text{dissipation}}{\dfrac{\sqrt{\alpha}\dot{\varepsilon}^{gp}_{kl}\varepsilon^r_{kl}}{k_r(\varepsilon^e_v + \varepsilon_c)}\dfrac{1}{\sqrt{\varepsilon^r_{st}\varepsilon^r_{st}}}\varepsilon^r_{ij}} & \dot{\varepsilon}^{gp}_{kl}\varepsilon^r_{kl} \geq 0 \\ \dot{\varepsilon}^{gp}_{ij} & \dot{\varepsilon}^{gp}_{kl}\varepsilon^r_{kl} < 0 \end{cases} \quad (11)$$

where the dissipation term is derived under the presumption that at the critical states ($\dot{\varepsilon}^{gp}_v = 0$ and $\varepsilon_c = 0$), $\sqrt{\varepsilon^r_{st}\varepsilon^r_{st}} = k_r\varepsilon^e_v/\sqrt{\alpha} = k_r\varepsilon^e_s$ with a material constant k_r, as will be discussed in the following section. The term $(\varepsilon^e_v + \varepsilon_c)$ in Eq. (11) also implies that larger ε^r_{ij} can be expected under a larger effective confining pressure and a higher magnitude of cohesion. In simulations, the initial value of residual elastic volumetric strain at a specific isotropic compression state is simply taken as $k_r(\varepsilon^e_{v0} + \varepsilon_c)$, where ε^e_{v0} is the initial elastic volumetric strain for the initial effective confining pressure.

Employing the thermodynamics, the following thermodynamic conjugates of ε_c and ε_{bs} should be defined to quantify the degradation laws of the cohesion and bond structure

$$p_c = \partial\omega_e/\partial\varepsilon_c, \qquad p_{bs} = \partial\omega_r/\partial\varepsilon_{bs} \quad (12)$$

where p_c and p_{bs} = degradation stresses that determine the degradations of cohesion and bond structure according to

$$\dot{\varepsilon}_c = -k_c\Theta\varepsilon_c p_c, \qquad \dot{\varepsilon}_{bs} = -k_{bs}\Theta\varepsilon_{bs}p_{bs} \quad (13)$$

where k_c and k_{bs} = parameters controlling the degradation rates of cohesion and bond structure, respectively.

The evolution of plastic and residual elastic strains [Eqs. (9) and (11)] and the bond degradation [Eq. (13)] will contribute to the energy dissipation of MICP-treated sand (see Supplemental Materials for details). In response to the resulting energy dissipation, the following simplified expression for the evolution of T_c can be defined for bonded and unbonded sands:

$$T_c = T_{ct}[1 - \tanh(k_0\sqrt[3]{\omega_e} - 3)]W_p/[2(W_p + a)] \quad (14)$$

where k_0 and a = material constants; and W_p = accumulated dissipated energy [Eqs. (S1)–(S5)]. The MICP bonding effect on T_c is naturally considered when Eq. (3) is substituted into Eq. (14), which is a simplified version of Eq. (S1). For MICP-treated sands at a free effective stress state ($\varepsilon_{ij}^e = 0$) with large W_p, there is an MICP bond-induced structural potential quantified by $\omega_e = \omega_0 = B(\varepsilon_{bs})^{m+2}/(m+2)$ and thus $T_c/T_{ct} \to [1 - \tanh(k_0\sqrt{\omega_0 3} - 3)]/2$, so that T_c reduces well below T_{ct}. Therefore, the MICP bonds prevent sands from being liquefied until the bond structure is fully destroyed under shearing.

Basic Model Features and Model Calibrations

Using the hyperelastic relationships of Eqs. (1) and (4), the inelastic strain laws of Eqs. (8), (9), and (11), the bonding degradation law of Eq. (13), and the granular configuration temperature relation of Eq. (14), the cyclic constitutive behavior of MICP bonded sand can be predicted. In this section, some basic model features will be discussed, from which the model calibration can also be clarified.

Hyperelasticity-Based State Boundary for Sands

The hyperelastic effective relationship presented in Eqs. (3) and (4) naturally restricts the effective stress state within a state boundary in stress space. With the third invariant of deviatoric elastic strain tensor considered, it will be able to account for the stress-induced anisotropy in the stress-strain hysteresis and state boundary of sands. To simplify the discussion hereafter, presumed loading paths in elastic strain space can be defined with a constant Lode angle θ defined by

$$\cos 3\theta = \sqrt{6}(\varepsilon_t^e/\varepsilon_s^e)^3 \tag{15}$$

which is 1 for triaxial compression and -1 for triaxial extension. The mean effective stress p' and generalized deviatoric stress q ($= \sqrt{S_{ij}S_{ij}}$, where S_{ij} is the deviatoric stress tensor) are then

$$p' = B(1 - T_c/T_{ct}) \times [(\varepsilon_v^e + \varepsilon_c)^m \varepsilon_v^e + m\xi(\varepsilon_v^e + \varepsilon_c)^{m-1}(\varepsilon_s^e)^2]$$
$$q = B(1 - T_c/T_{ct})\varepsilon_s^e \times \left[2\xi(\varepsilon_v^e + \varepsilon_c)^m + \theta(m+2)\cos 3\theta(\varepsilon_s^e)^m/\sqrt{6}\right] \tag{16}$$

Eq. (16) leads to pressure-dependent elastic stiffness for unbonded sands under isotropic stress conditions according to $[K_e, G_e] \propto (p')^{m/(m+1)}$, from which the nonlinear index m can be determined to simulate accurate elastic deformation. In the absence of measurements of the $[K_e, G_e]$-p' relationship, m is usually taken as a constant of 0.5 according to the work of Jiang and Liu (2003, 2004). It is assumed here that the value of m does not change due to the MICP cementation, which should be examined carefully by experimental tests in future studies.

In all cases, effective stress states of bonded and unbonded sands cannot surpass a state boundary in stress space as a natural theoretical result of Eq. (16). It corresponds to the states where the tangent elastic stiffness matrix $[H]$ in the incremental stress-strain relationship $\{dp'dq\}^T = [H]\{d\varepsilon_v^e d\varepsilon_s^e\}^T$ becomes singular, which requires the determinant

$$(\partial p'/\partial \varepsilon_v^e)(\partial q/\partial \varepsilon_s^e) - (\partial p'/\partial \varepsilon_s^e)(\partial q/\partial \varepsilon_v^e) = 0 \tag{17}$$

Figs. 1(a–c) show the predicted state boundary surface in principal stress space that transitions from a circular cone to a triangular cone when increasing the stress-induced anisotropy parameter ϑ from zero to a relatively large value. The stress-induced anisotropic strength can thus be observed and controlled by the parameter ϑ,

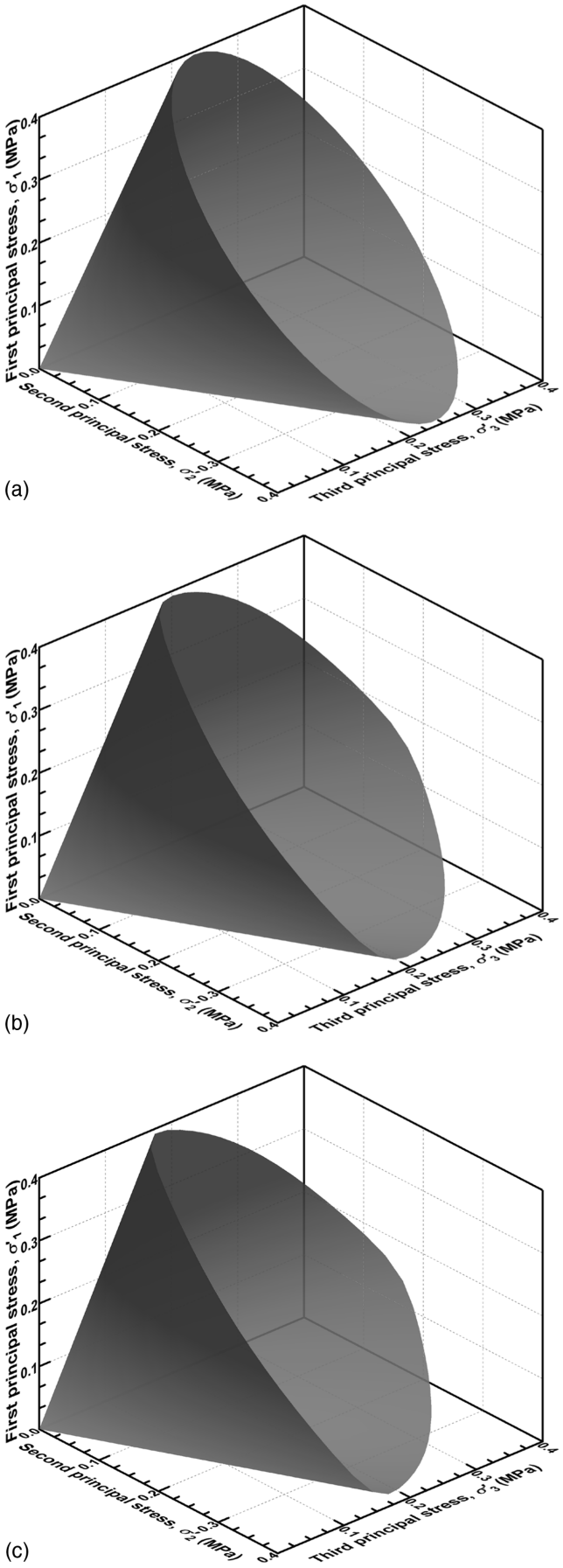

Fig. 1. State boundary surfaces in effective principal stress space: (a) $\theta = 0$; (b) $\theta = 0.05$; and (c) $\theta = 0.15$.

accompanied by a stress-induced anisotropy in elastic moduli according to Eq. (16).

MICP Reactant Index

In the model, the cohesion-related strain index ε_c and the bond structure index ε_{bs} are used to quantify the MICP bonding effects on the mechanical behavior of sands. The MICP will also decrease the void ratio of sands and thus increases their stiffness and strength. It is therefore essential to determine how a particular MICP treatment affects the dry density of sand and the magnitudes of ε_c and ε_{bs}. To this end, a reaction index for MICP treatment (Liu et al. 2019) is given as

$$R_c = V_c(C_c/C_a)^{k_m} \tag{18}$$

where V_c = reactant solution volume used for per unit volume of sand; $C_a(=1\ \text{mol/L})$ = standard concentration for normalization; C_c = concentration of reactant solution; and $k_m(=1.8)$ = constant power index for R_c (Liu et al. 2019). Details regarding the MICP reactant solution can be found in Xiao et al. (2019a). The R_c values of MICP-treated specimens are summarized in Table S1.

MICP-Improved Density and Strength

The variation of $CaCO_3$ mass precipitated per unit volume of sand, i.e., the increased density ρ_c, varies as a linear function of R_c, as shown in Fig. 2(a). The effect of MICP on the elastic stiffness and strength of sand can be considered by substitution of $\rho = \rho_0 + \rho_c$ into Eq. (5), where ρ_0 is the dry density of sand without MICP treatment. However, considering that only the $CaCO_3$ precipitated in contact regions between particles has major effects on the mechanical behavior of sand (DeJong et al. 2010; Al Qabany and Soga 2013; Cheng et al. 2013; Martinez et al. 2013; Soon et al. 2014; Gowthaman et al. 2019; Mahawish et al. 2019; Lin et al. 2020), this will lead to a certain extent of overevaluation of MICP effects. For this reason, instead of employing the real dry density, an equivalent dry density of sand treated with MICP should be defined for the state variable ρ throughout the model. To this end, it can be defined as

$$\rho = \rho_0 + 0.11\chi_\rho R_c \tag{19}$$

where a reduction coefficient χ_ρ denotes the proportion of the effective $CaCO_3$ to the total precipitated $CaCO_3$. Based on the undrained critical state strength increment of MICP-treated calcareous sand to untreated calcareous sand (Liu et al. 2019), the effective

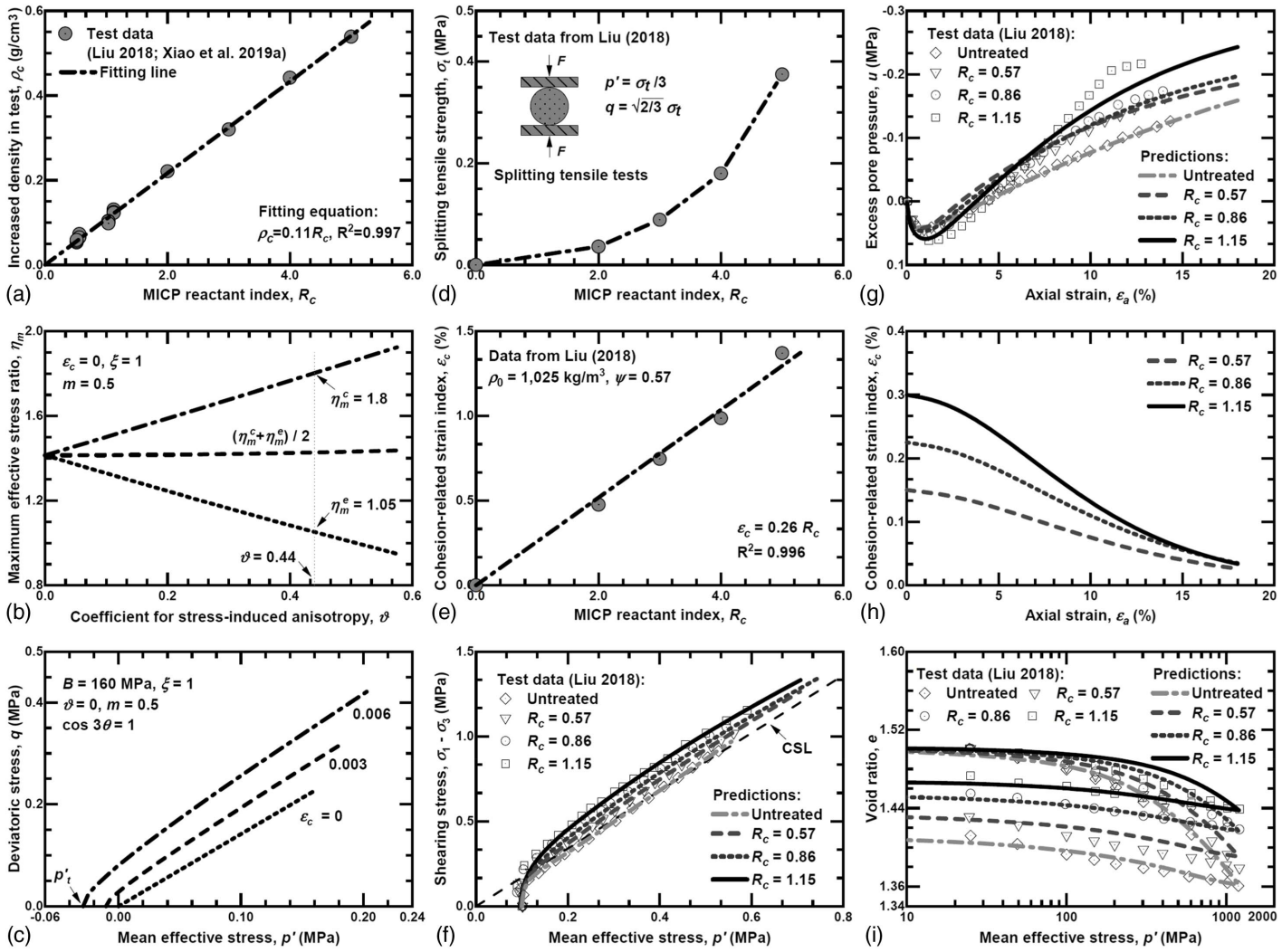

Fig. 2. (a) Relationship between increased density and MICP reaction index; (b–e) relationships for state boundary; and (f–i) predictions and validations for MICP-treated sand in monotonic loading.

$CaCO_3$ increment can be determined, and thereby an average value (0.57) of χ_ρ is adopted based on the ratio of the effective $CaCO_3$ increment to the observed total $CaCO_3$ increment in density. Table S1 lists the ρ values of MICP-treated specimens.

Then, the initial ε_c and ε_{bs} before loading can be defined as a linear function of R_c as follows:

$$\varepsilon_c = m_1 R_c, \qquad \varepsilon_{bs} = m_2 R_c \tag{20}$$

where m_1 and m_2 = two coefficients.

Critical State Based on the Proposed Model

At critical state, shear strain develops continuously under constant effective stress and density, i.e., $\dot{\varepsilon}_v = 0$, $\dot{\varepsilon}^e_{ij} = 0$, $\dot{\varepsilon}^r_{ij} = 0$, and hence $\dot{\varepsilon}^{gp}_{ij} = \dot{\varepsilon}_{ij}$. During shear loading, the cohesion ε_c and the bond structure index ε_{bs} will be fully degraded at critical states so that eventually $\varepsilon_c = 0$ and $\varepsilon_{bs} = 0$. Additionally, the critical granular configuration temperature should be at its minimum level corresponding to a critical state density, i.e., $T_{c\text{-}cs} = 0$ when Eq. (14) is adopted (the case in this study). Thus, from Eqs. (8), (9), and (11), $\varepsilon^r_{v\text{-}cs} = 0$ and

$$\sqrt{(e^e_{ij} - e^r_{ij})(e^e_{ij} - e^r_{ij})}(\varepsilon^e_v)^m|_{cs} = 1/\lambda_s$$
$$\varepsilon^e_{s-cs}/\varepsilon^e_{v-cs} = 1/\sqrt{\alpha}, \qquad \varepsilon^r_{s\text{-}cs}/\varepsilon^e_{v\text{-}cs} = \frac{k_r}{\sqrt{\alpha}} \tag{21}$$

where the subscript cs = corresponding value at the critical state. Under triaxial conditions, the first equation in Eq. (21) can be simplified to

$$(\varepsilon^e_{v-cs})^m \varepsilon^e_{s-cs} = 1/[\lambda_s(1-k_r)] \tag{22}$$

Substituting Eqs. (21) and (22) into Eq. (16), the CSL of sand can be described by

$$\frac{q_{cs}}{p'_{cs}} = \frac{2\xi + (m+2)\theta\cos 3\theta/(\sqrt{6}\alpha^{m/2})}{\sqrt{\alpha} + m\xi/\sqrt{\alpha}}$$
$$q_{cs} = \frac{B_0 e^{k\rho}}{\lambda_s(1-k_r)}\left(2\xi + \frac{m+2}{\sqrt{6}\alpha^{m/2}}\theta\cos 3\theta\right) \tag{23}$$

Eq. (20) shows that both the critical shear strength and the slope of CSL depend on the Lode angle.

Model Parameter Calibrations

The proposed model contains 14 model parameters. Their detailed calibrations are presented in the following sections.

Four Parameters for Elasticity

For unbonded sands, the state boundary in q-p' space is simply a straight line through the origin, the slope of which is defined as the maximum effective stress ratio, η_m (= $(q/p')_m$). The parameters η^c_m and η^e_m are the values of η_m for triaxial compression and extension, respectively. It can be derived that $\eta_m = (\xi/m)^{0.5}$ for all Lode angles without stress-induced anisotropy ($\theta = 0$). Based on η^c_m of 1.8 and η^e_m of 1.05 from the experimental data (Liu 2018; Xiao et al. 2019a), the ξ value of 1 can be estimated from the equation, $(\eta^c_m + \eta^e_m)/2 \approx (\xi/m)^{0.5}$ [Fig. 2(b)]. Based on $\xi = 1$ and $\varepsilon_c = 0$, the variation of η_m with θ for unbonded sand can be obtained. As shown in Fig. 2(b), η^c_m increases with θ and η^e_m decreases with θ, leading to more significant stress-induced anisotropy. Consequently, θ of 0.44 is determined based on $\eta^c_m = 1.8$ or $\eta^e_m = 1.05$.

From Eq. (23), $\ln q_{cs} \propto k\rho$, and thus $k = 0.00615$ m^3/kg is determined as the CSL slope in the $\ln q_{cs}$ - ρ space from the triaxial tests reported by Liu (2018). With k determined, B_0 can then be calibrated according to the hyperelastic relationship for an isotropic compression-rebound test of the unbonded sand compressed to a mean effective stress of p' and a dry density of ρ; that is, $B_0 = p' e^{-k\rho}(\varepsilon^e_v)^{-(m+1)}$, where ε^e_v is estimated as the volumetric strain recovered during the rebound test. Therefore, B_0 of 0.32 MPa is determined for the calcareous sand based on the test data from Liu (2018).

Six Parameters for Plasticity

Noting that parameters ξ and ϑ have been determined according to the hyperelasticity, the slope of CSL in the q - p' space is only a function of α [Eq. (23)]. For the calcareous sand used in this study, the α value of 3 is determined based on the undrained cyclic shear tests (Xiao et al. 2019a), leading to a change in the CSL slope from 1.24 for triaxial compression to 0.86 for triaxial extension. The parameter $k_r (\in (0, 1])$ in the model affects the stress-strain hysteretic loops, especially in one-way undrained cyclic shearing. Thus, k_r of 0.6 is suggested empirically to predict the magnitude of the cumulative axial strain (Xiao et al. 2019a). Based on a specific critical state obtained by Liu (2018), $\lambda_s(1-k_r) = 320$ is calculated for calcareous sand by Eq. (23). Thus, the λ_s value of 800 is determined, as k_r of 0.6 has already been obtained. The parameter λ_v determines the tendency of plastic dilation/contraction [Eq. (9)], and its empirical range is from $\lambda_s/3$ to λ_s. The parameter λ_v is then calibrated as 450 according to the dilation data of unbonded calcareous sand (Liu 2018). Meanwhile, at the critical state, k_0 of 0.38 Pa$^{-1/3}$ is determined by Eqs. (3), (14), and (28), with $T_c = T_{c\text{-}cs} = 0$. The parameter a ranges from 100 to 1,000 kJ/m^3. The a value of 350 kJ/m^3 is calibrated based on the two-way cyclic test data on the magnitude of the cumulative axial strain (Xiao et al. 2019a).

Four Parameters for Bonding

The parameters m_1 and m_2 represent the extent of MICP treatment in the improvement of cohesion strength and bond structure, respectively. Both m_1 and m_2 empirically range from 0 to 1% in the current study. For the MICP-treated sand, as shown in Fig. 2(c), the state boundary line (SBL) in q-p' space will no longer be a linear line through the origin but a curve perpendicular to the p' axis with an ultimate isotropic tensile strength p'_t determined by

$$p'_t = B_0 e^{k\rho} m^m [\varepsilon_c/(m+1)]^{m+1} \tag{24}$$

Due to the degradation of cohesion, ε_c is decreased in response to shearing so that the state boundary varies accordingly. However, upon tensile loading, it is realistic to presume that ε_c only changes slightly before the ultimate tensile strength is reached.

Table 1. Main parameters for MICP-treated calcareous sand

Parameters	Symbols	Values	Unit
Elasticity	ξ	1	—
	θ	0.44	—
	B_0	0.32	MPa
	k	0.00615	m^3/kg
Plasticity	α	3	—
	k_r	0.6	—
	λ_s	800	—
	λ_v	450	—
	k_0	0.38	Pa$^{-1/3}$
	a	350	kJ/m^3
Bonding	m_1	0.26	%
	m_2	0.8	%
	k_c	5×10^{-4}	Pa^{-1} s^{-1}
	k_{bs}	1×10^{-4}	Pa^{-1} s^{-1}

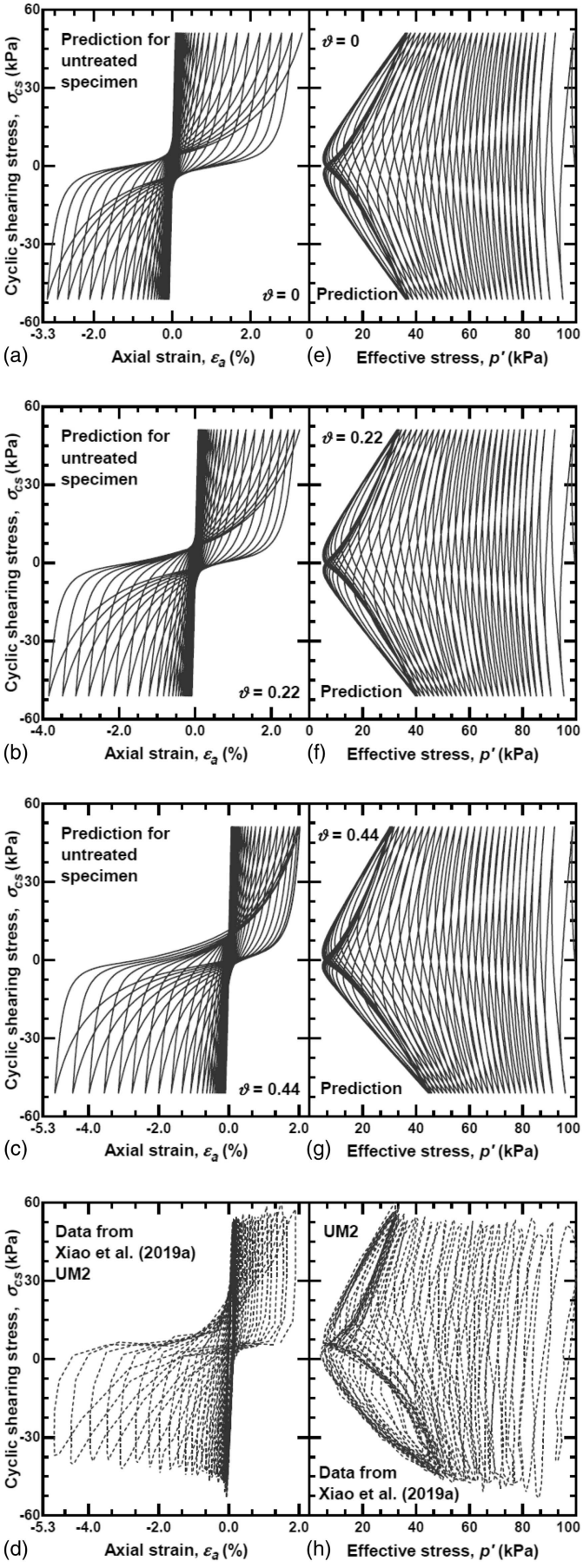

Fig. 3. Predictions and test results on untreated specimen: (a–d) σ_{cs}-ε_a relationship; and (e–h) σ_{cs}-p' relationship.

Therefore, Eq. (24) can be used to determine the initial ε_c-R_c relationship for MICP-treated sand defined in Eq. (20). Noting that it is usually difficult to implement an isotropic tensile test, the tensile strength σ_t from uniaxial or splitting tensile tests can be used instead. With a given σ_t, ε_c can be calculated by combining Eqs. (16) and (17) with the conditions of $p' = \sigma_t/3$ and $q = \sqrt{2/3}\sigma_t$. Accordingly, the ε_c-R_c relationship is determined using the measured σ_t-R_c relationship for MICP-treated calcareous sands [Fig. 2(d)], resulting in a slope coefficient of $m_1 = 0.26\%$ for the linear ε_c-R_c function [Eq. (20)], as shown in Fig. 2(e). It can be assumed that T_c of bonded sand under free stress state decreases to zero (approximated by $k_0\sqrt{\omega_0 3} - 3 = 3$) at a reference R_c and a reference ρ (denoted as R_{cr} and ρ_r, respectively). Thus, m_2 can be derived as

$$m_2 = (1/R_{cr})[6^3(m+2)/(B_0 k_0^3 e^{k\rho_r})]^{1/(m+2)} \tag{25}$$

where $R_{cr} = 2$ and $\rho_r = 1{,}125$ kg/m^3 from the tests (Liu 2018). The m_2 value of 0.8% is obtained, as all other parameters in Eq. (25) have already been calibrated.

The two remaining parameters, k_c and k_{bs}, control the degradation rates of the cohesion and the bond structure, respectively. It should be noted that following full degradation of cohesion due to the destruction of bonds, the angular bond (precipitated $CaCO_3$) particles (abraded from or remaining on the sand particles) continue to provide a significant magnitude of friction and interlocking within the previously bonded material. However, one can still expect that, under continuous shearing after bond breakage, the

Table 2. Details for the simulation cases (two-way cyclic shear)

No.	σ_d	ε_{c0}	ε_{bs0}	CSR
UL1	33	0	0	0.167
UL2	29	0	0	0.146
UL3	27	0	0	0.135
UL4	25	0	0	0.125
UM1	56	0	0	0.281
UM2	50	0	0	0.250
UM3	38	0	0	0.188
UM4	33	0	0	0.167
UM5	29	0	0	0.146
UD1	83	0	0	0.417
UD2	67	0	0	0.333
UD3	58	0	0	0.292
UD4	50	0	0	0.250
T1L1	58	0.146	0.411	0.292
T1L2	50	0.146	0.411	0.25
TlL3	42	0.146	0.411	0.208
TlL4	38	0.146	0.411	0.188
T1M1	67	0.134	0.379	0.333
TlM2	58	0.134	0.379	0.292
TlM3	50	0.134	0.379	0.25
TlM4	42	0.134	0.379	0.208
T2L1	92	0.291	0.822	0.458
T2L2	83	0.291	0.822	0.417
T2L3	75	0.291	0.822	0.375
T2L4	67	0.291	0.822	0.333
T2M1	100	0.269	0.758	0.5
T2M2	92	0.269	0.758	0.458
T2M3	83	0.269	0.758	0.417
T2M4	75	0.269	0.758	0.375
T2M5	67	0.269	0.758	0.333

Note: U = untreated sand specimens; L, M, and D = loose, medium-dense, and dense sand specimens, respectively; and Tl and T2 = specimens with low and high MICP cementation, respectively. The confining pressure σ_c' of all specimens is 100 kPa. The unit of σ_d is kPa.

angular bond particles can be gradually polished and/or fractured due to the high interparticle shearing stresses, leading to the complete loss of the initial bond structure (i.e., $\varepsilon_{bs} = 0$) (O'Donnell and Kavazanjian 2015). Therefore, $k_c > k_{bs}$ can be taken to enable a greater rate of cohesion degradation in simulations, where the empirical ranges of k_c and k_{bs} are from 1×10^{-4} to 10×10^{-4} $\text{Pa}^{-1}\,\text{s}^{-1}$ and from 0.5×10^{-4} to 1.5×10^{-4} $\text{Pa}^{-1}\,\text{s}^{-1}$, respectively. The parameters k_c and k_{bs} can finally be calibrated by trial and error based on the undrained triaxial compression tests (Liu 2018) and the undrained cyclic shear tests (Xiao et al. 2019a) on MICP-treated calcareous sand, respectively. Finally, the values of the 14 calibrated model parameters are summarized in Table 1.

Model Performances and Preverifications

Sand characterized with greater R_c exhibits greater dilation and critical shear strength due to the increase in dry density in Figs. 2(f and g), resulting in a development of larger negative excess pore pressure in Fig. 2(g). In addition, the predicted effective stress paths eventually tend to return to the CSL [Fig. 2(f)] with degradation of cohesion in Fig. 2(h), providing evidence of the presumption that both the cohesion and the bond structure will finally disappear due to shearing. The data for the cases of $R_c = 0$ and 0.57 in Figs. 2(f–h) and the case of $R_c = 0$ in Fig. 2(i) (for the calibration of B_0) are used to determine the previously discussed parameters. The data for the cases of $R_c = 0.86$ and 1.15 in Figs. 2(f–h) and the cases of $R_c = 0.57$, 0.86, and 1.15 in Fig. 2(i) are used to validate the model. The predictions by this model are consistent with the experimental data, indicating the validity of the calibrated model.

The state boundary and critical state features discussed previously enable the predictions of basic, monotonic mechanical behaviors of sands and provide the fundamental basis for modeling the cyclic behaviors. The elastic bulk and shear moduli described by hyperelasticity are also dependent on density and effective confining pressure, which could be one of the mechanisms for the stiffness degradation of sands subjected to undrained cyclic shear.

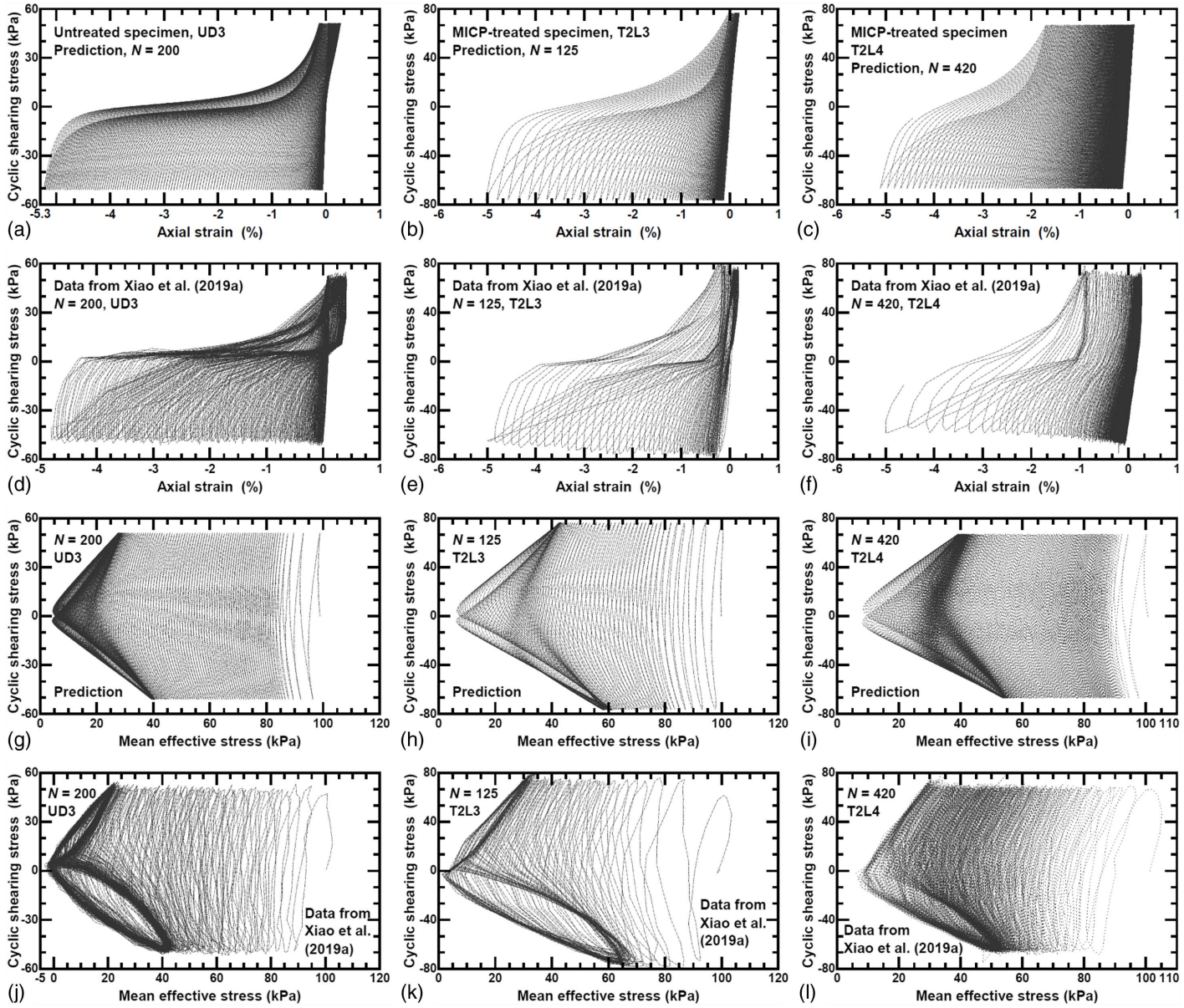

Fig. 4. Comparison between predictions and test results: (a–f) σ_{cs}-ε_a relationship for untreated and MICP-treated sand; and (g–l) σ_{cs}-p' relationship for untreated and MICP-treated sand.

More importantly, the concepts of residual stress (or equivalently the residual elastic strain) and granular configuration temperature are proposed in the model to capture both the pre- and postliquefaction behaviors of sands. In Eq. (9), the increase in residual elastic deviatoric strain e_{ij}^r during cyclic shearing according to Eq. (11) provides additional resistance to cyclic shearing deformation with more residual potential or stress generated. On the other hand, the cyclic increase in T_c to higher levels according to Eq. (14) results in postliquefaction deformation with accumulated stiffness degradation and strain accumulation according to Eqs. (4) and (9). This can be supported by the typical simulation results of undrained cyclic tests and the corresponding evolution of T_c and evolution of residual stresses shown in Fig. S1, where the cyclic shearing stress σ_{cs} is defined as $\sigma_{cs} = \sigma_a - \sigma_l$ (σ_a is the axial stress and σ_l is the lateral stress in a specimen).

Further considering the stress-induced anisotropy of calcareous sand, both the cyclic stress-strain relationship and the effective stress path show a different pattern from the isotropic case, as shown in Figs. 3(a–h). The cyclic stress-strain loops in Figs. 3(a–c) gradually shift to the extension side with increasing θ due to the dependence of the hyperelastic parameter θ on stress anisotropy. It is shown that for the calcareous sand in this study, the calibrated θ value of 0.44 mentioned before can sufficiently capture the experimental responses, as shown in Figs. 3(c, d, g, and h).

Model Predictions and Verifications

General Information

The cyclic behavior predicted by the proposed model using the calibrated values of 14 parameters is examined through a comprehensive comparison to the cyclic response of MICP-treated calcareous sand reported by Xiao et al. (2019a). The comparisons will validate the model and examine the effects of cohesion degradation, bond structure degradation, initial density, and MICP bonding on cyclic shear behaviors of sand. Details regarding the simulation cases are summarized in Table 2, including the amplitude of cyclic shearing stress σ_d and the cyclic stress ratio ($CSR = 0.5\sigma_d/\sigma_c'$, where σ_c' is the confining pressure). The initial cohesion-related strain index ε_{c0} is determined according to the MICP reaction index as described in Eq. (17), and the initial bond structure index ε_{bs0} is calculated using Eq. (18) with $m_2 = 0.8\%$, $R_{cr} = 2$, and $\rho_r = 1.125$ g/cm^3.

Figs. 4(a–l) show comparisons between the simulations and experimentally observed cyclic response of untreated and MICP-treated calcareous sand, in which N represents the cycle number. In general, the cyclic stress-strain hysteresis and effective stress path are well reproduced by the proposed model. In particular, the differences in responses between the compression and extension cycles are well captured. Differences in response between the simulations and the experiments are most notable in the cyclic extension excursions. Cyclic triaxial test results are well known to exhibit the effects of platen separation and specimen necking for large CSRs and axial strains (Seed et al. 1983). In this regard, the simulations may better represent the cyclic response than the experiments.

Notably, sand specimens with different void ratios and bonding levels would show different failure mechanisms that are consistent with the accumulation of strain and generation of excess pore pressure. Especially, the cyclic anisotropic strain accumulation can be captured for both treated and untreated calcareous sands under different dry densities and CSRs; that is, in all cases, the accumulation of strain is biased to the extension side as a result of the stress-induced anisotropy described in both the hyperelasticity and the plasticity. This is also supported by the predicted cyclic strain histories of untreated and MICP-treated, loose and medium-dense calcareous sands, as given in Fig. S2.

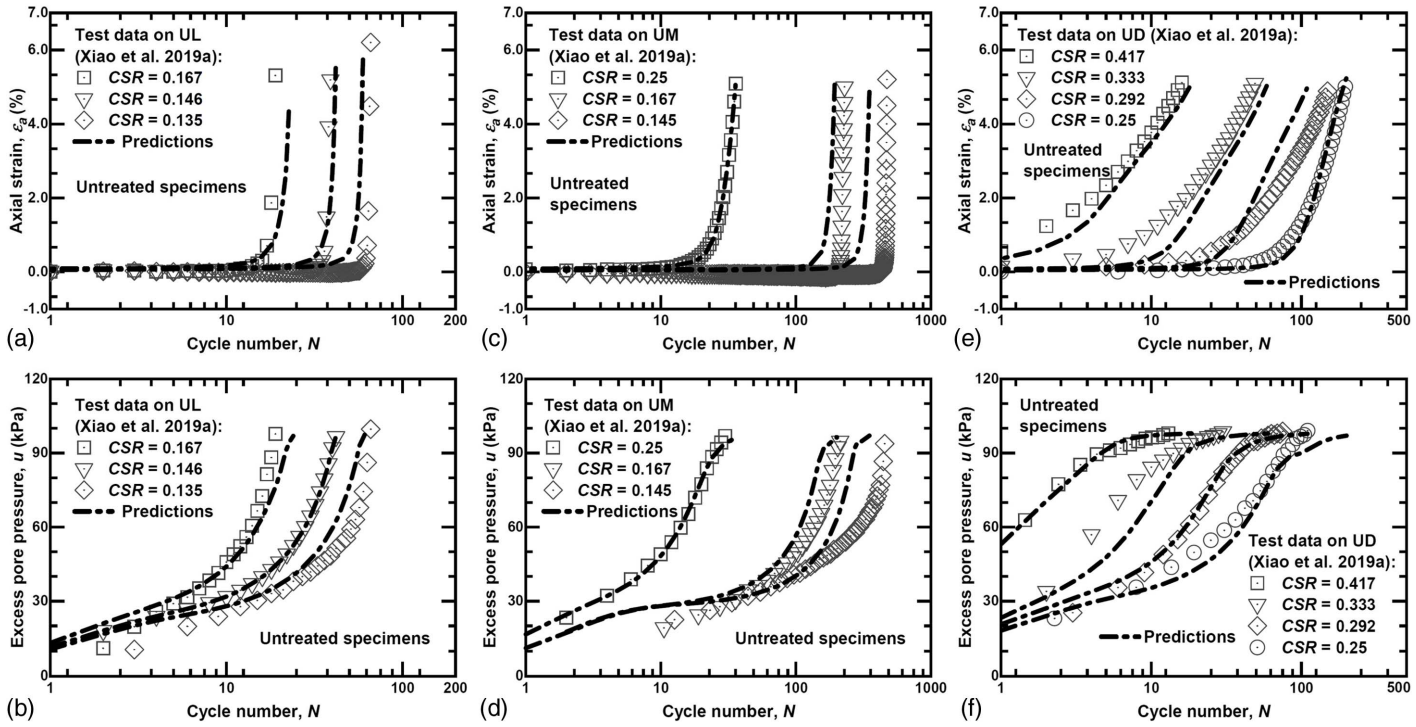

Fig. 5. Evolution of axial strain and excess pore pressure with shear stress cycles of untreated calcareous sands: (a and b) initial low density; (c and d) initial medium-dense density; and (e and f) initial density.

J. Geotech. Geoenviron. Eng., 2021, 147(12): 04021149

Cyclic Behavior of Untreated Calcareous Sand

The cyclic behavior of untreated calcareous sand largely depends on the initial dry density, the effective confining pressure, and the cyclic shear stress amplitude (Xiao et al. 2019a). Typical prediction results for unbonded specimens can be found in Fig. 4 as well as in Fig. S3. Figs. 5(a–f) compare the observed and simulated strain and excess pore pressure for the unbonded calcareous sand specimens. It is shown that the loose and medium-dense specimens sheared under different *CSR*s exhibit similar failure patterns, in which a fast increase in the accumulated strain is triggered at a certain cycle number and the pore pressure continuously increases to its maximum. On the contrary, dense sand specimens sheared under a high *CSR* exhibit a gradually decreasing rate of excess pore pressure generation as the effective stress path approaches the failure state, resulting in a more progressive pattern of strain accumulation. Furthermore, specimens of the same dry density sheared under the same confining pressure exhibit an initial period of low pore pressure development as the *CSR* decreases, which is captured by the model simulations. On the whole, these model predictions for density and *CSR* effects on the cyclic strain accumulation and generation of excess pore pressure are consistent with the experimental data.

Effects of Biocementation on Cyclic Behavior

The effects of biocementation on the undrained cyclic behavior of sand are attributed to the increase in dry density, the cohesion, and the bond structure, all of which tend to increase the cyclic resistance of sand. During cyclic loading, the effect of an MICP-induced increase in density is constant, whereas the effects of cohesion and bond structure will eventually vanish due to cyclic degradation. It is therefore important to associate such mechanisms with the evolution of strain and effective stress. As shown in Figs. 6(a–d), the cyclic shear strength of medium-dense calcareous sand is markedly improved by increasing R_c from 0.56 to 1.03, with the cycle number required for generating an axial strain of 5% on the extension side increasing from 23 to 200. Figs. 6(a–d) also show that the anisotropy of strain accumulation is increased by the bonding effects. With a high MICP-treatment level, the strain of medium-dense calcareous sand sheared with $\sigma_d = 67$ kPa accumulates almost entirely on the extension side and the cyclic stress-strain hysteresis shifts to the extension side after a certain number of cycles.

Comparison of the development of strain before and after the first encounter with the failure envelope (i.e., CSL) on the extension side indicates two different strain mechanisms. In order to better interpret the underlying mechanisms, Figs. 6(e–h) present the evolution of the normalized cohesion-related strain index $\varepsilon_c/\varepsilon_{c0}$ and the normalized bond structure index $\varepsilon_{bs}/\varepsilon_{bs0}$ with the normalized cyclic number N/N_L, where N_L is defined as the cycle number required to trigger liquefaction. For the case of T1M1, both ε_c and ε_{bs} are nearly fully degraded at the time that the effective stress path touches the CSL at $N = 13$ [Fig. 6(b)], resulting in a cyclic behavior similar to that of an unbonded sand, thus leading to the accumulation of strain at a relatively high rate. On the contrary, for the case of T2M5, in which the R_c is larger and a larger initial value of ε_c and ε_{bs} is used, the failure line is first reached at $N = 60$ with a small extensional strain of 0.16% [Fig. 6(c)]. Although ε_c has been degraded to a low magnitude at this point, the bond structure parameter ε_{bs} is degraded only slightly [Fig. 6(h)], so that the sand continues to deform more like a solid with a corresponding granular configuration temperature far from the threshold temperature. That is why in the T2M5 case, a low level of strain accumulation is maintained for a large number of cycles after $N = 60$, and why relatively significant strain accumulation in the same case is observed at the

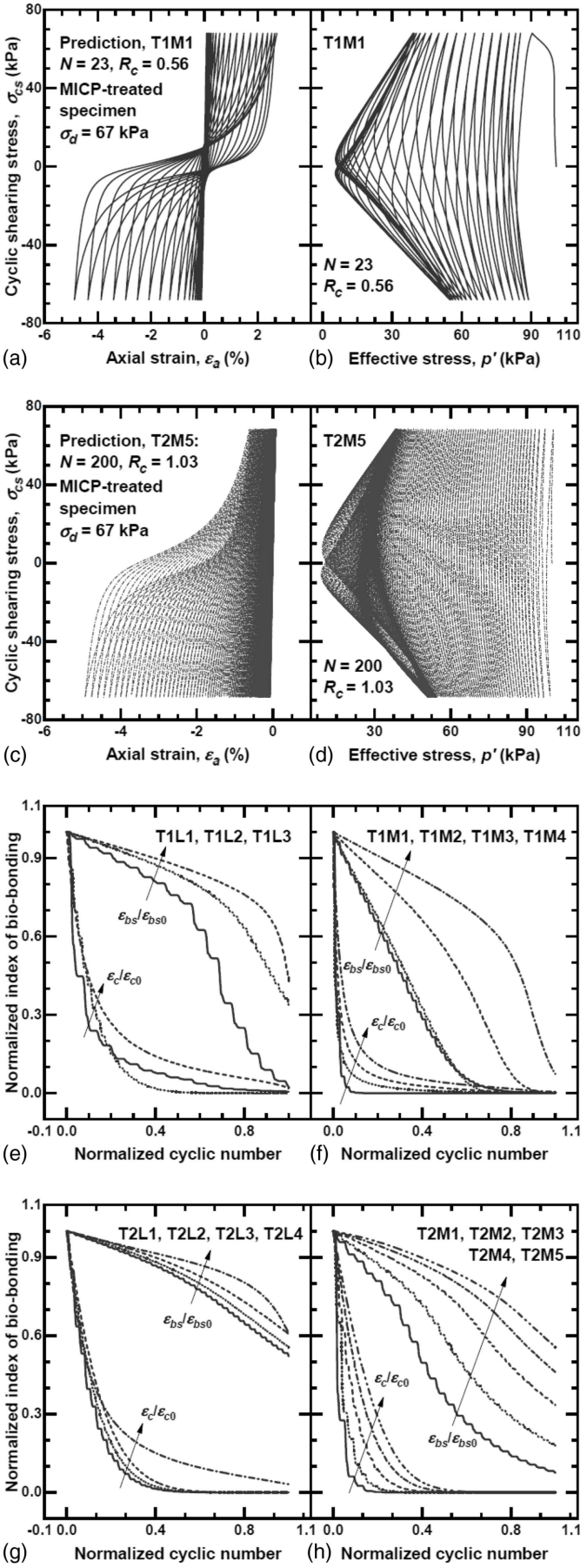

Fig. 6. (a–d) Prediction of the cyclic behavior; and (e–h) evolution of the cohesion or structure index with cyclic number.

end of simulation when the bond structure is degraded gradually to a low level. Therefore, the degradation of cohesion and bond structure can be regarded as the fundamental mechanisms of cyclic resistance in the cyclic response of bonded sands. More importantly, as shown in Figs. 6(e–h), all the simulation cases show a two-stage degradation of the bonding effects: in Stage 1 the cohesion is fully or largely degraded, and in Stage 2 the bond structure is destroyed gradually or rapidly (depending on R_c, dry density, and CSR). In all cases, the effective stress paths of the bonded sands rarely surpass the final CSL determined for the corresponding unbonded case, indicating that the cohesion should degrade first. However, once the cohesion is fully degraded, there are still sufficient structural effects from the interlocking and friction inside the precipitated $CaCO_3$ particles fractured in shearing, which can only be fully destroyed due to shearing in Stage 2. From the modeling perspective, such a two-stage cyclic bonding degradation can be captured by appropriate calibration of the parameters governing the degradation of cohesion and bond structure in Eq. (12).

Figs. 7(a–h) compare the simulated and measured results of strain and excess pore pressure generation in MICP-treated calcareous sand. In general, the cyclic behavior of the MICP-treated sand is well captured by the proposed model. The results of the simulations are used to generate the CSR-N_L relationships for the different treatment cases, as shown in Fig. 7(i). The cyclic shear strength area between CSR-N_L curves for loose and medium-dense calcareous sands is shifted up by the low-level MICP treatment, and the sand specimens in the cases of T1L have similar cyclic shear strengths as the medium-dense unbonded sand (UM). With a high level of MICP bonding, this shear strength area is remarkably shifted above the CSR-N_L curve for the dense unbonded sand (see the curves for T2L and T2M). However, the loose sand specimens bonded with $R_c = 1.12$ have even higher cyclic strengths than the medium-dense specimens bonded with a slightly lower R_c of 1.03, which corresponds to both smaller ε_c and ε_{bs}. This indicates that, with the increase of MICP-treatment level, the cyclic strength is mainly controlled by the MICP bonding rather than the initial unbonded conditions.

Comparing the cases of T1 and T2 in Figs. 7(a–d), it is clear that the patterns of pore pressure development could be different between weakly and strongly bonded specimens. Depending on the CSR, three stages of excess pore pressure generation can be observed in the predicted responses for those specimens corresponding to strongly bonded cases (e.g., T2L-0.333, T2M-0.333, and T2M-0.375), including (1) a stage of rapid increase during early cycles, (2) the quasi-stable stage of relatively constant-rate increase in excess pore pressure, and followed by (3) the rapid failure to

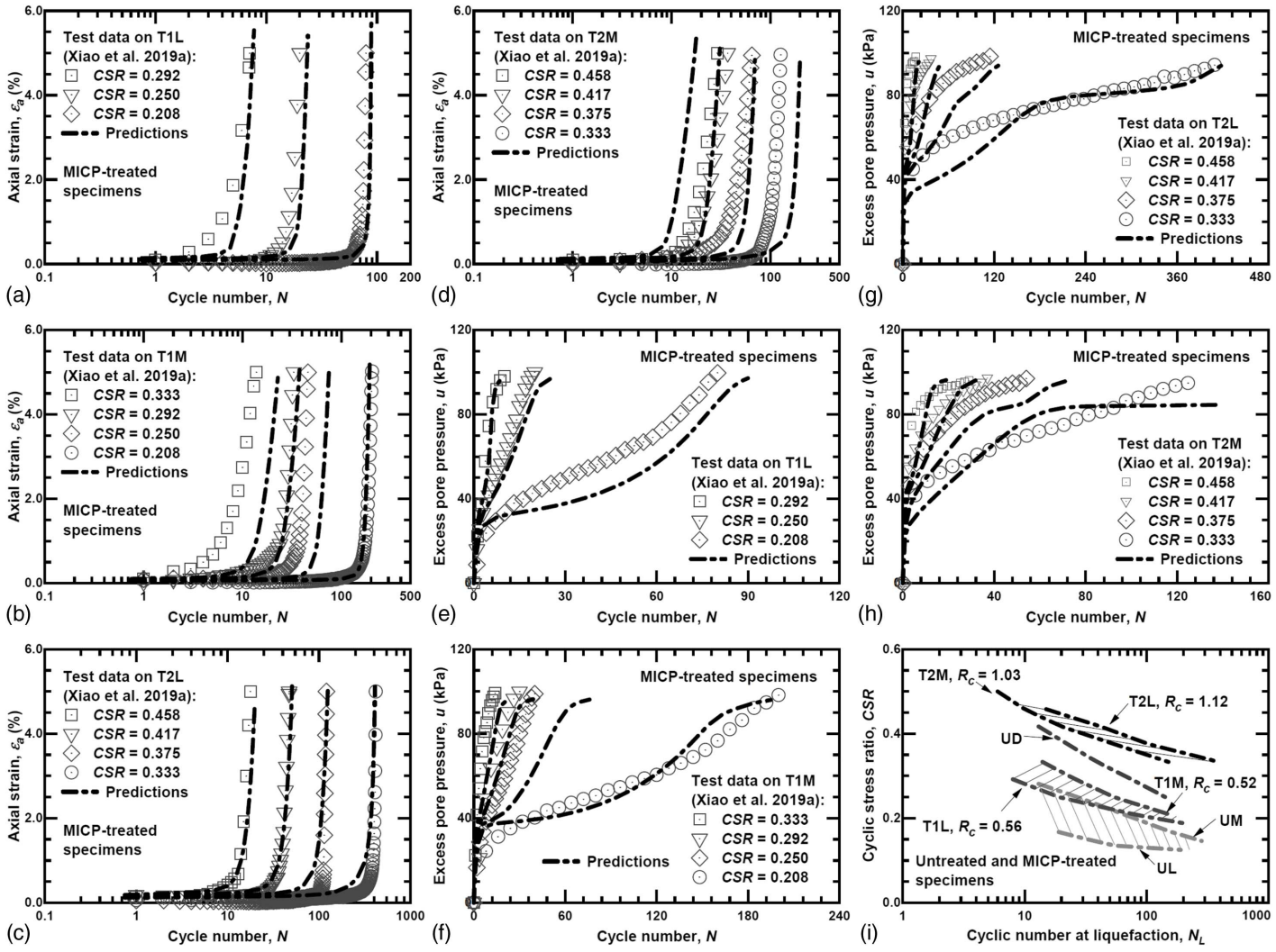

Fig. 7. Comparisons between model predictions and test results of MICP-treated specimens with different densities and CSRs: (a–d) axial strain development; (e–h) excess pore pressure; and (i) comparison of model predictions of the CSR-N_L relationship for untreated and MICP-treated specimens.

J. Geotech. Geoenviron. Eng., 2021, 147(12): 04021149

liquefaction. From Figs. 6(g and h), most of the degradation in cohesion is completed in Stage 1; however, the bond structure continues to contribute to stability during Stage 2, leading to a quasi-stable stage with excess pore pressure developing slowly. This quasi-stable period may be maintained for a large number of cycles, particularly for specimens subjected to lower *CSR*s, prior to the rapid degradation of the bond structure that leads to Stage 3, manifested by an accelerated increase in the rate of excess pore pressure. Due to the degradations of cohesion and the associated bond structure, all of the bonded specimens in Figs. 7(a–d) exhibit a smaller strain accumulation during the early cycles but a sharper increase in the strain accumulation to failure than the unbonded dense (UD) specimens in Fig. 5(e), which exhibit similar *CSR*s (e.g., 0.417 of UD1 versus 0.458 of T2L1 or 0.458 of T2M2).

In order to demonstrate the prediction accuracy quantitatively, the error in the predicted number (N_ε) of cycles required to generate a given cumulative axial strain ε_a is presented in Fig. 8 for the comparison between experimental and predicted results shown in Figs. 5 and 7 for both unbonded and bonded specimens. Noting that the logarithm of cycle number is usually used in evaluating the cyclic responses of soils (Truong et al. 2021), the logarithmic error of N_ε is used here, i.e., $R_{\Delta N\varepsilon} = |\ln(N_\varepsilon^p/N_\varepsilon^m)|/\ln N_\varepsilon^m$, where N_ε^p and N_ε^m are the predicted and measured N_ε, respectively. It is demonstrated in Fig. 8 that for most cases large errors are only observed for an initial cycle number corresponding to an axial strain smaller than 0.5%. Although the model should be improved to address accuracy for these small-strain amplitudes, the error in N_ε decreases to 10% or smaller for axial strain >0.5%. Exceptions include cases of T2M2 and T2M5 (with large-strain error ranging from 10% to 20%) and cases of T1M4, UM2, and UD1 (with large-strain error of about 30%). In general, most of the predictions are consistent with the experimental results and suggest that the model represents a promising approach for capturing the cyclic response of biotreated sands.

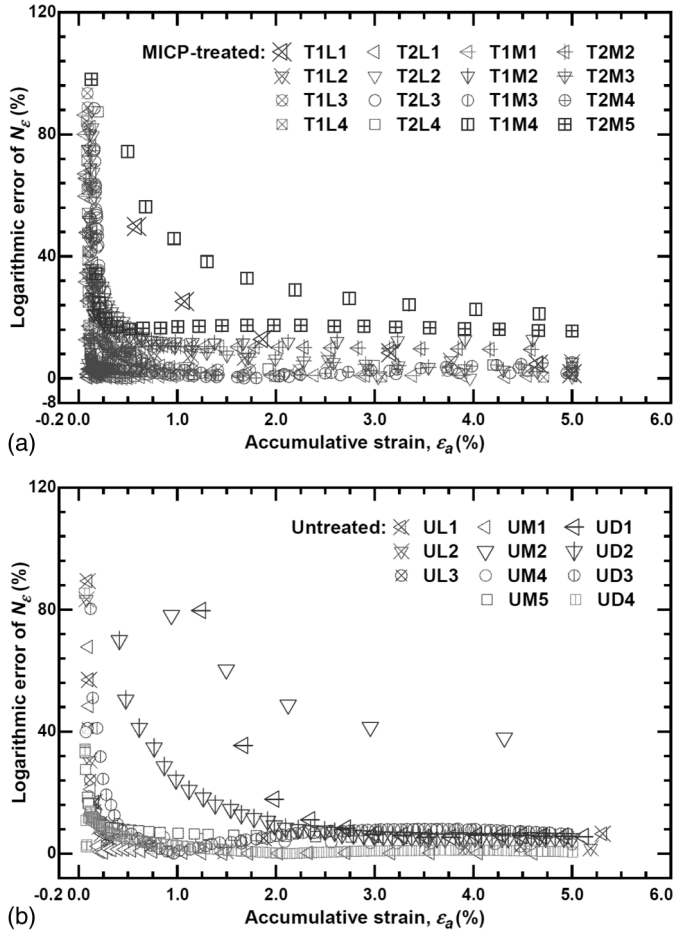

Fig. 8. Variation of prediction errors of N_ε with axial strain in undrained cyclic simulations: (a) MICP-treated specimens; and (b) untreated specimens.

Conclusion

In this paper, a cyclic constitutive model is developed for MICP-treated calcareous sands based on the nonlinear hyperelasticity- and thermodynamics-based plasticity. The main conclusions are summarized as follows:

1. In this model, the macroelastic potential and the residual elastic potential are defined for MITP-treated sands, leading to nonlinear hyperelastic relations that account for stress-induced anisotropy, cohesion, and bond (precipitated $CaCO_3$) structure. Then, the hyperelasticity is coupled with thermodynamic plasticity. Significantly, the concepts of granular configuration entropy and temperature are incorporated into the hyperelastic-plastic formulation to account for the effects of particle configuration evolution on the cyclic behavior of sand. Using such an approach, the cyclic behavior of both untreated and MICP-treated sands can be well predicted by the model without concepts such as yield surface, plastic potential surface, loading/unloading criterion, and mapping rules, which helps to decrease the complexity and number of parameters in the cyclic constitutive model.
2. The undrained cyclic behavior of untreated sand can be attributed to the state-dependent elastic modulus based on hyperelasticity, the storage and relaxation of residual elastic potential, and the evolution of granular configuration temperature. The residual elastic potential and hence the residual stress can be stored and relaxed due to the nonelastic deformation, providing additional resistance of the sand to plastic deformation and forming the hysteretic stress-strain loops in both one-way and two-way cyclic shear loadings. During this process, the granular configuration temperature gradually increases and approaches the threshold value at which the sand loses all elasticity, finally leading to liquefaction. The stress-induced anisotropy of the SBL and that of the CSL are also considered.
3. An MICP reactant index is defined in this study to couple the details of MICP treatment with the cyclic model. The MICP bonding effects on the cyclic behavior of sand are interpreted by the increased dry density, the cohesion, and the bond structure. It is shown that a two-stage cyclic degradation of bonding effects should be reproduced in a cyclic constitutive model for MICP-treated sands, in which the bond structure is able to be kept at a high level even after the cohesion is fully degraded due to cyclic shear loads. This can be regarded as the fundamental mechanism underlying the cyclic behavior of sands treated with different MICP-treatment levels. The anisotropy of strain accumulation on compression and extension sides can be predicted by the model, depending on the initial untreated dry density, the cyclic stress ratio, and the MICP-treatment level. The model also captures that the cyclic shear strength of bonded sand is mainly controlled by the MICP-treatment level, particularly for high MICP-treatment levels. In general, the model is well validated by predicting the strain and excess-pore-pressure developments of untreated and MICP-treated calcareous sands subjected to different undrained cyclic shear loads.

Data Availability Statement

All data, models, and code generated or used during the study appear in the published article and the Supplemental Materials online.

Acknowledgments

The authors would like to acknowledge the National Science Foundation of China (Grant Nos. 51922024, 51978104, and 52078085) and the Chongqing Science and Technology Commission (Grant No. cstc2017jcyjAX0061). TME was supported by the US National Science Foundation (CMMI-1933355) during the course of this work. This support is gratefully acknowledged.

Supplemental Materials

Table S1, Figs. S1–S3, and Eqs. (S1)–(S5) are available online in the ASCE Library (www.ascelibrary.org).

References

Al Qabany, A., and K. Soga. 2013. "Effect of chemical treatment used in MICP on engineering properties of cemented soils." *Géotechnique* 63 (4): 331–339. https://doi.org/10.1680/geot.SIP13.P.022.

Al Qabany, A., K. Soga, and C. Santamarina. 2012. "Factors affecting efficiency of microbially induced calcite precipitation." *J. Geotech. Geoenviron. Eng.* 138 (8): 992–1001. https://doi.org/10.1061/(ASCE)GT.1943-5606.0000666.

Bardet, J. P. 1990. "Lode dependences for isotropic pressure-sensitive elastoplastic materials." *J. Appl. Mech.* 57 (9): 498–506. https://doi.org/10.1115/1.2897051.

Barrero, A. R., M. Taiebat, and Y. F. Dafalias. 2020. "Modeling cyclic shearing of sands in the semifluidized state." *Int. J. Numer. Anal. Methods Geomech.* 44 (3): 371–388. https://doi.org/10.1002/nag.3007.

Baudet, B., and S. Stallebrass. 2004. "A constitutive model for structured clays." *Géotechnique* 54 (4): 269–278. https://doi.org/10.1680/geot.2004.54.4.269.

Cheng, L., R. Cord-Ruwisch, and M. A. Shahin. 2013. "Cementation of sand soil by microbially induced calcite precipitation at various degrees of saturation." *Can. Geotech. J.* 50 (1): 81–90. https://doi.org/10.1139/cgj-2012-0023.

Collins, I. F. 2005. "The concept of stored plastic work or frozen elastic energy in soil mechanics." *Géotechnique* 55 (5): 373–382. https://doi.org/10.1680/geot.2005.55.5.373.

Cui, M., J. Zheng, R. Zhang, H. Lai, and J. Zhang. 2017. "Influence of cementation level on the strength behaviour of bio-cemented sand." *Acta Geotech.* 12 (5): 971–986. https://doi.org/10.1007/s11440-017-0574-9.

Dafalias, Y. F., and E. P. Popov. 1976. "Plastic internal variables formalism of cyclic plasticity." *J. Appl. Mech.* 43 (4): 645–651. https://doi.org/10.1115/1.3423948.

Darby, K. M., G. L. Hernandez, J. T. DeJong, R. W. Boulanger, M. G. Gomez, and D. W. Wilson. 2019. "Centrifuge model testing of liquefaction mitigation via microbially induced calcite precipitation." *J. Geotech. Geoenviron. Eng.* 145 (10): 04019084. https://doi.org/10.1061/(ASCE)GT.1943-5606.0002122.

DeJong, J. T., M. B. Fritzges, and K. Nüsslein. 2006. "Microbially induced cementation to control sand response to undrained shear." *J. Geotech. Geoenviron. Eng.* 132 (11): 1381–1392. https://doi.org/10.1061/(ASCE)1090-0241(2006)132:11(1381).

DeJong, J. T., B. M. Mortensen, B. C. Martinez, and D. C. Nelson. 2010. "Bio-mediated soil improvement." *Ecol. Eng.* 36 (2): 197–210. https://doi.org/10.1016/j.ecoleng.2008.12.029.

Duo, L., T. Kan-Liang, Z. Hui-Li, W. Yu-Yao, N. Kang-Yi, and Z. Shi-Can. 2018. "Experimental investigation of solidifying desert aeolian sand using microbially induced calcite precipitation." *Constr. Build. Mater.* 172 (May): 251–262. https://doi.org/10.1016/j.conbuildmat.2018.03.255.

Evans, T. M., and C. B. Brown. 2014. "Microstates and macrostructures for granular assemblies." In *Proc., Geo-Characterization and Modeling for Sustainability*, 2858–2866. Reston, VA: ASCE.

Evans, T. M., and J. D. Frost. 2010. "Multiscale investigation of shear bands in sand: Physical and numerical experiments." *Int. J. Numer. Anal. Methods Geomech.* 34 (15): 1634–1650. https://doi.org/10.1002/nag.877.

Fattahi, S. M., A. Soroush, and N. Huang. 2020. "Biocementation control of sand against wind erosion." *J. Geotech. Geoenviron. Eng.* 146 (6): 04020045. https://doi.org/10.1061/(ASCE)GT.1943-5606.0002268.

Feng, K., and B. M. Montoya. 2016. "Influence of confinement and cementation level on the behavior of microbial-induced calcite precipitated sands under monotonic drained loading." *J. Geotech. Geoenviron. Eng.* 142 (1): 04015057. https://doi.org/10.1061/(ASCE)GT.1943-5606.0001379.

Feng, K., and B. M. Montoya. 2017. "Quantifying level of microbial-induced cementation for cyclically loaded sand." *J. Geotech. Geoenviron. Eng.* 143 (6): 06017005. https://doi.org/10.1061/(ASCE)GT.1943-5606.0001682.

Gao, Y., L. Hang, J. He, and J. Chu. 2019. "Mechanical behaviour of bio-cemented sands at various treatment levels and relative densities." *Acta Geotech.* 14 (3): 697–707. https://doi.org/10.1007/s11440-018-0729-3.

Gomez, M. G., J. T. DeJong, and C. M. Anderson. 2018. "Effect of bio-cementation on geophysical and cone penetration measurements in sands." *Can. Geotech. J.* 55 (11): 1632–1646. https://doi.org/10.1139/cgj-2017-0253.

Gomez, M. G., C. E. Hunt, B. C. Martinez, J. T. Dejong, D. W. Major, and S. M. Dworatzek. 2015. "Field-scale bio-cementation tests to improve sands." *Proc. Inst. Civ. Eng. Ground Improv.* 168 (3): 206–216. https://doi.org/10.1680/grim.13.00052.

Gowthaman, S., S. Mitsuyama, K. Nakashima, M. Komatsu, and S. Kawasaki. 2019. "Biogeotechnical approach for slope soil stabilization using locally isolated bacteria and inexpensive low-grade chemicals: A feasibility study on Hokkaido expressway soil, Japan." *Soils Found.* 59 (2): 484–499. https://doi.org/10.1016/j.sandf.2018.12.010.

Groot, S. D., and P. Mazur. 1962. *Non-equilibrium thermodynamics*. Amsterdam, Netherlands: North-Holland Publishing Company.

He, J., Y. Gao, Z. Gu, J. Chu, and L. Wang. 2020. "Characterization of crude bacterial urease for $CaCO_3$ precipitation and cementation of silty sand." *J. Mater. Civ. Eng.* 32 (5): 04020071. https://doi.org/10.1061/(ASCE)MT.1943-5533.0003100.

Houlsby, G. T., A. Amorosi, and E. Rojas. 2005. "Elastic moduli of soils dependent on pressure: A hyperelastic formulation." *Géotechnique* 55 (5): 383–392. https://doi.org/10.1680/geot.2005.55.5.383.

Jefferies, M. 1997. "Plastic work and isotropic softening in unloading." *Géotechnique* 47 (5): 1037–1042. https://doi.org/10.1680/geot.1997.47.5.1037.

Jiang, N.-J., and K. Soga. 2017. "The applicability of microbially induced calcite precipitation (MICP) for internal erosion control in gravel–sand mixtures." *Géotechnique* 67 (1): 42–55. https://doi.org/10.1680/jgeot.15.P.182.

Jiang, N.-J., K. Soga, and M. Kuo. 2017. "Microbially induced carbonate precipitation for seepage-induced internal erosion control in sand–clay mixtures." *J. Geotech. Geoenviron. Eng.* 143 (3): 04016100. https://doi.org/10.1061/(ASCE)GT.1943-5606.0001559.

Jiang, N.-J., C.-S. Tang, L.-Y. Yin, Y.-H. Xie, and B. Shi. 2019. "Applicability of microbial calcification method for sandy-slope surface erosion control." *J. Mater. Civ. Eng.* 31 (11): 04019250. https://doi.org/10.1061/(ASCE)MT.1943-5533.0002897.

Jiang, Y., and M. Liu. 2003. "Granular elasticity without the Coulomb condition." *Phys. Rev. Lett.* 91 (14): 144301. https://doi.org/10.1103/PhysRevLett.91.144301.

Jiang, Y., and M. Liu. 2004. "Energetic instability unjams sand and suspension." *Phys. Rev. Lett.* 93 (14): 148001. https://doi.org/10.1103/PhysRevLett.93.148001.

Kasama, K., H. Ochiai, and N. Yasufuku. 2000. "On the stress-strain behaviour of lightly cemented clay based on an extended critical state concept." *Soils Found.* 40 (5): 37–47. https://doi.org/10.3208/sandf.40.5_37.

Lee, K., D. Chan, and K. Lam. 2004. "Constitutive model for cement treated clay in a critical state framework." *Soils Found.* 44 (3): 69–77. https://doi.org/10.3208/sandf.44.3_69.

Li, M., L. Li, U. Ogbonnaya, K. Wen, A. Tian, and F. Amini. 2016. "Influence of fiber addition on mechanical properties of MICP-treated sand." *J. Mater. Civ. Eng.* 28 (4): 04015166. https://doi.org/10.1061/(ASCE)MT.1943-5533.0001442.

Li, S., C. Li, D. Yao, and S. Wang. 2020. "Feasibility of microbially induced carbonate precipitation and straw checkerboard barriers on desertification control and ecological restoration." *Ecol. Eng.* 152 (Jun): 105883. https://doi.org/10.1016/j.ecoleng.2020.105883.

Li, X. S., and Y. F. Dafalias. 2012. "Anisotropic critical state theory: Role of fabric." *J. Eng. Mech.* 138 (3): 263–275. https://doi.org/10.1061/(ASCE)EM.1943-7889.0000324.

Lin, H., M. T. Suleiman, and D. G. Brown. 2020. "Investigation of pore-scale $CaCO_3$ distributions and their effects on stiffness and permeability of sands treated by microbially induced carbonate precipitation (MICP)." *Soils Found.* 60 (4): 944–961. https://doi.org/10.1016/j.sandf.2020.07.003.

Lin, H., M. T. Suleiman, D. G. Brown, and E. Kavazanjian Jr. 2016. "Mechanical behavior of sands treated by microbially induced carbonate precipitation." *J. Geotech. Geoenviron. Eng.* 142 (2): 04015066. https://doi.org/10.1061/(ASCE)GT.1943-5606.0001383.

Liu, L. 2018. "Experimental study on mechanical properties of MICP-treated calcareous sand." Ph.D. thesis, Dept. of Civil and Transportation Engineering, Hohai Univ.

Liu, L., H. Liu, A. W. Stuedlein, T. M. Evans, and Y. Xiao. 2019. "Strength, stiffness, and microstructure characteristics of biocemented calcareous sand." *Can. Geotech. J.* 56 (10): 1502–1513. https://doi.org/10.1139/cgj-2018-0007.

Liu, S., R. Wang, J. Yu, X. Peng, Y. Cai, and B. Tu. 2020. "Effectiveness of the anti-erosion of an MICP coating on the surfaces of ancient clay roof tiles." *Constr. Build. Mater.* 243 (May): 118202. https://doi.org/10.1016/j.conbuildmat.2020.118202.

Ma, G., X. He, X. Jiang, H. Liu, J. Chu, and Y. Xiao. 2021. "Strength and permeability of bentonite-assisted biocemented coarse sand." *Can. Geotech. J.* 58 (7): 969–981. https://doi.org/10.1139/cgj-2020-0045.

Mahawish, A., A. Bouazza, and W. P. Gates. 2018. "Effect of particle size distribution on the bio-cementation of coarse aggregates." *Acta Geotech.* 13 (4): 1019–1025. https://doi.org/10.1007/s11440-017-0604-7.

Mahawish, A., A. Bouazza, and W. P. Gates. 2019. "Unconfined compressive strength and visualization of the microstructure of coarse sand subjected to different biocementation levels." *J. Geotech. Geoenviron. Eng.* 145 (8): 04019033. https://doi.org/10.1061/(ASCE)GT.1943-5606.0002066.

Manzari, M. T., and Y. F. Dafalias. 1997. "A critical state two-surface plasticity model for sands." *Géotechnique* 47 (2): 255–272. https://doi.org/10.1680/geot.1997.47.2.255.

Martinez, B. C., J. T. DeJong, T. R. Ginn, B. M. Montoya, T. H. Barkouki, C. Hunt, B. Tanyu, and D. Major. 2013. "Experimental optimization of microbial-induced carbonate precipitation for soil improvement." *J. Geotech. Geoenviron. Eng.* 139 (4): 587–598. https://doi.org/10.1061/(ASCE)GT.1943-5606.0000787.

Montoya, B. M., and J. T. DeJong. 2015. "Stress-strain behavior of sands cemented by microbially induced calcite precipitation." *J. Geotech. Geoenviron. Eng.* 141 (6): 04015019. https://doi.org/10.1061/(ASCE)GT.1943-5606.0001302.

Montoya, B. M., J. T. DeJong, and R. W. Boulanger. 2013. "Dynamic response of liquefiable sand improved by microbial-induced calcite precipitation." *Géotechnique* 63 (4): 302–312. https://doi.org/10.1680/geot.SIP13.P.019.

Mroz, Z. 1967. "On the description of anisotropic workhardening." *J. Mech. Phys. Solids* 15 (3): 163–175. https://doi.org/10.1016/0022-5096(67)90030-0.

Mujah, D., M. A. Shahin, and L. Cheng. 2017. "State-of-the-art review of biocementation by microbially induced calcite precipitation (MICP) for soil stabilization." *Geomicrobiol. J.* 34 (6): 524–537. https://doi.org/10.1080/01490451.2016.1225866.

Naeimi, M., and J. Chu. 2017. "Comparison of conventional and bio-treated methods as dust suppressants." *Environ. Sci. Pollut. Res. Int.* 24 (29): 23341–23350. https://doi.org/10.1007/s11356-017-9889-1.

Nafisi, A., B. M. Montoya, and T. M. Evans. 2020. "Shear strength envelopes of biocemented sands with varying particle size and cementation level." *J. Geotech. Geoenviron. Eng.* 146 (3): 04020002. https://doi.org/10.1061/(ASCE)GT.1943-5606.0002201.

Nafisi, A., S. Safavizadeh, and B. M. Montoya. 2019. "Influence of microbe and enzyme-induced treatments on cemented sand shear response." *J. Geotech. Geoenviron. Eng.* 145 (9): 06019008. https://doi.org/10.1061/(ASCE)GT.1943-5606.0002111.

O'Donnell, T. S., and E. Kavazanjian Jr. 2015. "Stiffness and dilatancy improvements in uncemented sands treated through MICP." *J. Geotech. Geoenviron. Eng.* 141 (11): 02815004. https://doi.org/10.1061/(ASCE)GT.1943-5606.0001407.

O'Donnell, T. S., B. E. Rittmann, and E. Kavazanjian Jr. 2017a. "MIDP: Liquefaction mitigation via microbial denitrification as a two-stage process. I: Desaturation." *J. Geotech. Geoenviron. Eng.* 143 (12): 04017094. https://doi.org/10.1061/(ASCE)GT.1943-5606.0001818.

O'Donnell, T. S., B. E. Rittmann, and E. Kavazanjian, Jr. 2017b. "MIDP: Liquefaction mitigation via microbial denitrification as a two-stage process. II: MICP." *J. Geotech. Geoenviron. Eng.* 143 (12): 04017095. https://doi.org/10.1061/(ASCE)GT.1943-5606.0001806.

Palmer, A. C. 1967. "Stress-strain relations for clays: An energy theory." *Géotechnique* 17 (4): 348–358. https://doi.org/10.1680/geot.1967.17.4.348.

Pastor, M., O. C. Zienkiewicz, and A. H. C. Chan. 1990. "Generalized plasticity and the modelling of soil behaviour." *Int. J. Numer. Anal. Methods Geomech.* 14 (3): 151–190. https://doi.org/10.1002/nag.1610140302.

Pham, V. P., L. A. van Paassen, W. R. L. van der Star, and T. J. Heimovaara. 2018. "Evaluating strategies to improve process efficiency of denitrification-based MICP." *J. Geotech. Geoenviron. Eng.* 144 (8): 04018049. https://doi.org/10.1061/(ASCE)GT.1943-5606.0001909.

Porcino, D. D., and V. Marcianò. 2017. "Bonding degradation and stress–dilatancy response of weakly cemented sands." *Geomech. Geoeng.* 12 (4): 221–233. https://doi.org/10.1080/17486025.2017.1347287.

Preisler, Z., and M. Dijkstra. 2016. "Configurational entropy and effective temperature in systems of active Brownian particles." *Soft Matter* 12 (28): 6043–6048. https://doi.org/10.1039/C6SM00889E.

Rahimi, M., D. Chan, and A. Nouri. 2016. "Bounding surface constitutive model for cemented sand under monotonic loading." *Int. J. Geomech.* 16 (2): 04015049. https://doi.org/10.1061/(ASCE)GM.1943-5622.0000534.

Riveros, G. A., and A. Sadrekarimi. 2020a. "Effect of microbially induced cementation on the instability and critical state behaviours of Fraser River sand." *Can. Geotech. J.* 57 (2): 1870–1880. https://doi.org/10.1139/cgj-2019-0514.

Riveros, G. A., and A. Sadrekarimi. 2020b. "Liquefaction resistance of Fraser River sand improved by a microbially-induced cementation." *Soil Dyn. Earthquake Eng.* 131 (Apr): 106034. https://doi.org/10.1016/j.soildyn.2020.106034.

Rouainia, M., and D. Muir Wood. 2000. "A kinematic hardening constitutive model for natural clays with loss of structure." *Géotechnique* 50 (2): 153–164. https://doi.org/10.1680/geot.2000.50.2.153.

Salifu, E., E. Maclachlan, K. R. Iyer, C. W. Knapp, and A. Tarantino. 2016. "Application of microbially induced calcite precipitation in erosion mitigation and stabilisation of sandy soil foreshore slopes: A preliminary investigation." *Eng. Geol.* 201 (Feb): 96–105. https://doi.org/10.1016/j.enggeo.2015.12.027.

Sasaki, T., and R. Kuwano. 2016. "Undrained cyclic triaxial testing on sand with non-plastic fines content cemented with microbially induced $CaCO_3$." *Soils Found.* 56 (3): 485–495. https://doi.org/10.1016/j.sandf.2016.04.014.

Seed, H., I. Idriss, and I. Arango. 1983. "Evaluation of liquefaction potential using field performance data." *J. Geotech. Eng.* 109 (3): 458–482. https://doi.org/10.1061/(ASCE)0733-9410(1983)109:3(458).

Simatupang, M., M. Okamura, K. Hayashi, and H. Yasuhara. 2018. "Small-strain shear modulus and liquefaction resistance of sand with carbonate precipitation." *Soil Dyn. Earthquake Eng.* 115 (Dec): 710–718. https://doi.org/10.1016/j.soildyn.2018.09.027.

Song, C. P., D. Elsworth, S. Zhi, and C. Y. Wang. 2021. "The influence of particle morphology on microbially induced $CaCO_3$ clogging in granular media." *Mar. Georesour. Geotechnol.* 39 (1): 74–81. https://doi.org/10.1080/1064119X.2019.1677828.

Soon, N. W., L. M. Lee, T. C. Khun, and H. S. Ling. 2014. "Factors affecting improvement in engineering properties of residual soil through microbial-induced calcite precipitation." *J. Geotech. Geoenviron. Eng.* 140 (5): 04014006. https://doi.org/10.1061/(ASCE)GT.1943-5606.0001089.

Suebsuk, J., S. Horpibulsuk, and M. D. Liu. 2010. "Modified structured Cam Clay: A generalised critical state model for destructured, naturally structured and artificially structured clays." *Comput. Geotech.* 37 (7): 956–968. https://doi.org/10.1016/j.compgeo.2010.08.002.

Suebsuk, J., S. Horpibulsuk, and M. D. Liu. 2011. "A critical state model for overconsolidated structured clays." *Comput. Geotech.* 38 (5): 648–658. https://doi.org/10.1016/j.compgeo.2011.03.010.

Terzis, D., and L. Laloui. 2019. "Cell-free soil bio-cementation with strength, dilatancy and fabric characterization." *Acta Geotech.* 14 (3): 639–656. https://doi.org/10.1007/s11440-019-00764-3.

Tian, K., Y. Wu, H. Zhang, D. Li, K. Nie, and S. Zhang. 2018. "Increasing wind erosion resistance of aeolian sandy soil by microbially induced calcium carbonate precipitation." *Land Degrad. Dev.* 29 (12): 4271–4281. https://doi.org/10.1002/ldr.3176.

Truong, M. H., B. Indraratna, T. T. Nguyen, J. Carter, and C. Rujikiatkamjorn. 2021. "Analysis of undrained cyclic response of saturated soils." *Comput. Geotech.* 134 (Jun): 104095. https://doi.org/10.1016/j.compgeo.2021.104095.

Uzuoka, R., A. Yashima, T. Kawakami, and J. M. Konrad. 1998. "Fluid dynamics based prediction of liquefaction induced lateral spreading." *Comput. Geotech.* 22 (3): 243–282. https://doi.org/10.1016/S0266-352X(98)00006-8.

Valanis, K. C., J. F. Peters, and J. Gill. 1993. "Configurational entropy, nonassociativity and uniqueness in granular media." *Acta Mech.* 100 (1–2): 79–93. https://doi.org/10.1007/BF01176863.

van Paassen, L. A. 2009. "Biogrout, ground improvement by microbial induced carbonate precipitation." Ph.D. thesis, Dept. of Geotechnology, Delft Univ. of Technology.

van Paassen, L. A., R. Ghose, T. J. M. van der Linden, W. R. L. van der Star, and M. C. M. van Loosdrecht. 2010. "Quantifying biomediated ground improvement by ureolysis: Large-scale biogrout experiment." *J. Geotech. Geoenviron. Eng.* 136 (12): 1721–1728. https://doi.org/10.1061/(ASCE)GT.1943-5606.0000382.

Wang, X. R., J. L. Tao, R. T. Bao, T. Tran, and S. Tucker-Kulesza. 2018. "Surficial soil stabilization against water-induced erosion using polymer-modified microbially induced carbonate precipitation." *J. Mater. Civ. Eng.* 30 (10): 04018267. https://doi.org/10.1061/(ASCE)MT.1943-5533.0002490.

Wang, Z., and F. Ma. 2019. "Bounding surface plasticity model for liquefaction of sand with various densities and initial stress conditions." *Soil Dyn. Earthquake Eng.* 127 (Dec): 105843. https://doi.org/10.1016/j.soildyn.2019.105843.

Wang, Z., J. Ma, H. Gao, A. W. Stuedlein, J. He, and B. Wang. 2020. "Unified thixotropic fluid model for soil liquefaction." *Géotechnique* 70 (10): 849–862. https://doi.org/10.1680/jgeot.17.P.300.

Whiffin, V. S. 2004. "Microbial $CaCO_3$ precipitation for the production of biocement." Ph.D. thesis, School of Biological Sciences and Biotechnology, Morduch Univ.

Whiffin, V. S., L. A. van Paassen, and M. P. Harkes. 2007. "Microbial carbonate precipitation as a soil improvement technique." *Geomicrobiol. J.* 24 (5): 417–423. https://doi.org/10.1080/01490450701436505.

Xiao, P., H. Liu, A. W. Stuedlein, T. M. Evans, and Y. Xiao. 2019a. "Effect of relative density and bio-cementation on the cyclic response of calcareous sand." *Can. Geotech. J.* 56 (12): 1849–1862. https://doi.org/10.1139/cgj-2018-0573.

Xiao, P., H. Liu, Y. Xiao, A. W. Stuedlein, and T. M. Evans. 2018. "Liquefaction resistance of bio-cemented calcareous sand." *Soil Dyn. Earthquake Eng.* 107 (Apr): 9–19. https://doi.org/10.1016/j.soildyn.2018.01.008.

Xiao, Y., H. Chen, A. W. Stuedlein, T. M. Evans, J. Chu, L. Cheng, N. Jiang, H. Lin, H. Liu, and H. M. Aboel-Naga. 2020a. "Restraint of particle breakage by biotreatment method." *J. Geotech. Geoenviron. Eng.* 146 (11): 04020123. https://doi.org/10.1061/(ASCE)GT.1943-5606.0002384.

Xiao, Y., H. Liu, Y. Chen, and J. Jiang. 2014. "Bounding surface plasticity model incorporating the state pressure index for rockfill materials." *J. Eng. Mech.* 140 (11): 04014087. https://doi.org/10.1061/(ASCE)EM.1943-7889.0000802.

Xiao, Y., A. W. Stuedlein, Z. Pan, H. Liu, T. M. Evans, X. He, H. Lin, J. Chu, and L. A. van Paassen. 2020b. "Toe bearing capacity of precast concrete piles through biogrouting improvement." *J. Geotech. Geoenviron. Eng.* 146 (12): 06020026. https://doi.org/10.1061/(ASCE)GT.1943-5606.0002404.

Xiao, Y., A. W. Stuedlein, J. Ran, T. M. Evans, L. Cheng, H. Liu, L. A. van Paassen, and J. Chu. 2019b. "Effect of particle shape on strength and stiffness of biocemented glass beads." *J. Geotech. Geoenviron. Eng.* 145 (11): 06019016. https://doi.org/10.1061/(ASCE)GT.1943-5606.0002165.

Xiao, Y., Y. Wang, C. S. Desai, X. Jiang, and H. Liu. 2019c. "Strength and deformation responses of biocemented sands using a temperature-controlled method." *Int. J. Geomech.* 19 (11): 04019120. https://doi.org/10.1061/(ASCE)GM.1943-5622.0001497.

Xiao, Y., Z. Zhang, and J. Wang. 2020c. "Granular hyperelasticity with inherent and stress-induced anisotropy." *Acta Geotech.* 15 (3): 671–680. https://doi.org/10.1007/s11440-019-00768-z.

Yan, W. M., and X. S. Li. 2011. "A model for natural soil with bonds." *Géotechnique* 61 (2): 95–106. https://doi.org/10.1680/geot.8.P.061.

Yang, Z., and A. Elgamal. 2008. "Multi-surface cyclic plasticity sand model with Lode angle effect." *Geotech. Geol. Eng.* 26 (3): 335–348. https://doi.org/10.1007/s10706-007-9170-3.

Yu, H. S., S. M. Tan, and F. Schnaid. 2007. "A critical state framework for modelling bonded geomaterials." *Geomech. Geoeng.* 2 (1): 61–74. https://doi.org/10.1080/17486020601164275.

Zamani, A., and B. M. Montoya. 2019. "Undrained cyclic response of silty sands improved by microbial induced calcium carbonate precipitation." *Soil Dyn. Earthquake Eng.* 120 (May): 436–448. https://doi.org/10.1016/j.soildyn.2019.01.010.

Zhang, J., and G. Wang. 2012. "Large post-liquefaction deformation of sand, Part I: Physical mechanism, constitutive description and numerical algorithm." *Acta Geotech.* 7 (2): 69–113. https://doi.org/10.1007/s11440-011-0150-7.

Zhang, Z. 2017. "A thermodynamics-based theory for thethermo-poromechanical modeling of saturated clay." *Int. J. Plast.* 92 (May): 164–185. https://doi.org/10.1016/j.ijplas.2017.03.007.

Zhang, Z., and X. Cheng. 2015. "A thermodynamic constitutive model for undrained monotonic and cyclic shear behavior of saturated soils." *Acta Geotech.* 10 (6): 781–796. https://doi.org/10.1007/s11440-015-0389-5.

Zhang, Z., L. Li, and Z. Xu. 2021. "A thermodynamics-based hyperelastic-plastic coupled model unified for unbonded and bonded soils." *Int. J. Plast.* 137 (Feb): 102902. https://doi.org/10.1016/j.ijplas.2020.102902.

Zheng, W. 2015. "A cyclic UH model for sand." *Earthquake Eng. Eng. Vibr.* 14 (2): 229–238. https://doi.org/10.1007/s11803-015-0019-0.

Ziotopoulou, A. K. 2014. "A sand plasticity model for earthquake engineering applications." Ph.D. thesis, Dept. of Civil and Environmental Engineering, Univ. of California Davis.